Astronomy & Astrophysics manuscript no. Lefever_11956
October 15, 2009

Spectroscopic determination of the fundamental parameters of 66 B-type stars in the field-of-view of the CoRoT satellite

K. Lefever[1,2], J. Puls[3], T. Morel[1,4], C. Aerts[1,5], L. Decin[1,⋆⋆], and M. Briquet[1,⋆]

1 Instituut voor Sterrenkunde, K.U. Leuven, Celestijnenlaan 200D, B-3001 Leuven, Belgium
2 BIRA-IASB, Ringlaan 3, B-1180 Brussel, Belgium
3 Universitätssternwarte München, Scheinerstr. 1, D-81679 München, Germany
4 Institut d'Astrophysique et de Géophysique, Université de Liège, Allée du 6 Août 17, Bât B5c, B-4000 Liège, Belgium
5 Departement Astrofysica, IMAPP, Radboud Universiteit Nijmegen, PO Box 9010, 6500 GL Nijmegen, the Netherlands

Received / Accepted

Abstract

Aims. We aim to determine the fundamental parameters of a sample of B stars with apparent visual magnitudes below 8 in the field-of-view of the CoRoT space mission, from high-resolution spectroscopy.
Methods. We developed an automatic procedure for the spectroscopic analysis of B-type stars with winds, based on an extensive grid of FASTWIND model atmospheres. We use the equivalent widths and/or the line profile shapes of continuum normalized hydrogen, helium and silicon line profiles to determine the fundamental properties of these stars in an automated way.
Results. After thorough tests, both on synthetic datasets and on very high-quality, high-resolution spectra of B stars for which we already had accurate values of their physical properties from alternative analyses, we applied our method to 66 B-type stars contained in the ground-based archive of the CoRoT space mission. We discuss the statistical properties of the sample and compare them with those predicted by evolutionary models of B stars.
Conclusions. Our spectroscopic results provide a valuable starting point for any future seismic modelling of the stars, should they be observed by CoRoT.

Key words. Stars: atmospheres – Stars: early-type – Stars: fundamental parameters – Methods: data analysis – Techniques: spectroscopic – Line: profiles

1. Introduction

The detailed spectroscopic analysis of B-type stars has for a long time been restricted to a limited number of targets. Reasons for this are the a priori need for a realistic atmosphere model, the lack of large samples with high-quality spectra, and the long-winded process of line profile fitting, as the multitude of photospheric and wind parameters requires a large parameter space to be explored.

The advent of high-resolution, high signal-to-noise spectroscopy in the nineties led to a renewed interest of the scientific community in spectroscopic research, and in particular in the relatively poorly understood massive stars. The establishment of continuously better instrumentation and the improvement in quality of the obtained spectroscopic data triggered a series of studies, which led to a rapid increase in our knowledge of massive stars. In this respect, it is not surprising to note that this is exactly the period where several groups started to upgrade their atmosphere prediction code for such stars, see, e.g., CMFGEN - Hillier & Miller (1998), PHOENIX - Hauschildt & Baron (1999), WM-Basic - Pauldrach et al. (2001), POWR - Gräfener et al. (2002) and FASTWIND - Santolaya-Rey et al. (1997), Puls et al. (2005). Initially, major attention was devoted to the establishment of a realistic atmosphere model (improvement of atomic data, inclusion of line blanketing and clumping), rather than analyzing large samples of stars.

Simultaneously with improvements in the atmosphere predictions, also the number of available high-quality data increased rapidly, mainly thanks to the advent of multi-object spectroscopy. At the time of writing, the largest survey is the VLT-FLAMES Survey of Massive Stars (Evans et al. 2005), containing over 600 Galactic, SMC and LMC B-type spectra[1] (in 7 different clusters), gathered over more than 100 hours of VLT time. The survey not only allowed to derive the stellar parameters and rotational velocities for hundreds of stars (Dufton et al. 2006; Hunter et al. 2008b), but also to study the evolution of surface N abundances and the effective tempera-

Send offprint requests to: Karolien.Lefever@aeronomie.be

⋆ Postdoctoral researcher of the Fund for Scientific Research of Flanders (FWO)

1 additionally, roughly 90 O-stars have been observed.

ture scales in the Galaxy and Magellanic Clouds (Trundle et al. 2007; Hunter et al. 2007, 2008a).

In preparation of the CoRoT space mission, and almost contemporary with the FLAMES setup, another large database was constructed: GAUDI (Ground-based Asteroseismology Uniform Database Interface, Solano et al. 2005). It gathers ground-based observations of more than 1500 objects, including high-resolution spectra of about 250 massive B-type stars, with the goal to determine their fundamental parameters as input for seismic modeling (see Section 3).

The availability of such large samples of B-type stars brings within reach different types of studies, e.g., they may lead to a significant improvement in the fundamental parameter calibration for this temperature range and to a confrontation with and evaluation of stellar evolution models (e.g., Hunter et al. 2008b). The drawback of this huge flood of data, however, is, as mentioned before, the large parameter space to be explored, which can be quite time-consuming, if no adequate method is available. It requires a method which is able to derive the complete set of parameters of stars with a wide variety of physical properties in an objective way.

To deal with the large GAUDI dataset, we investigated the possibility of *automated* spectral line fitting and we opted for a grid-based fitting method: AnalyseBstar. In Section 2, we justify our choice for a grid-based method, present its design and discuss several tests which were applied to check the performance of the routine. A more detailed description of our methodology can be found in the (online) appendix. Section 3 illustrates the first application of AnalyseBstar to the sample of CoRoT candidate targets in the GAUDI database and Section 4 deals with the physical interpretation and some statistical properties of the resulting parameters. Section 5 summarizes the main results obtained in this paper.

2. Automated fitting using a grid-based method

Spectral line fitting is a clear example of an optimization problem. To find the optimal fit to a given observed stellar spectrum among a set of theoretically predicted spectra emerging from stellar atmosphere models, requires scanning the parameter space spanned by the free parameters of the stellar atmosphere model. Due to the extent of this parameter space, and with the goal of analyzing large samples in mind, it is clear that performing the parameter scan through fit-by-eye is not the best option. The 'subjective' eye should be replaced by an 'intelligent' algorithm, in such way that the procedure of finding the optimum fit becomes automatic, objective, fast and reproducible, even though human intervention can never be excluded completely.

2.1. General description of our grid-based method

In contrast to the case of the O stars (e.g., Mokiem et al. 2005), treating the entire spectral range B with a single approach requires additional diagnostic lines besides H and He. In this region, Si (in its different ionization stages), rather than He, becomes the most appropriate temperature indicator. With this in mind, we have chosen to develop an automatic procedure which is based on an extensive and refined grid of FASTWIND models. This offers a good compromise between effort, time and precision if an *appropriate grid* has been set up. The grid should be comprehensive, as dense as possible and representative for the kind of objects one wants to analyze. Similar to a fit-by-eye method, a grid-based algorithm will follow an iterative scheme, but in a reproducible way using a goodness-of-fit parameter. Starting from a first guess for the fundamental parameters, based on spectral type and/or published information, improved solutions are derived by comparing line profiles resulting from well-chosen existing (i.e. pre-calculated) grid models to the observed line profiles. The algorithm terminates once the fit quality cannot be improved anymore by modifying the model parameters.

We are well aware of the limitations inherent to this method. As soon as a new version/update of the atmosphere or line synthesis code is released (e.g., due to improved atomic data), the grid needs to be updated as well. The advantage, on the other hand, is that the line-profile fitting method itself will remain and the job is done with the computation of a new grid. This is of course a huge work (e.g., seven months were needed to compute[2] and check the grid in Lefever et al. 2007a), but thanks to the fast performance of the FASTWIND code, this should not really be an insurmountable problem.

A grid-based method fully relies on a static grid and no additional models are computed to derive the most likely parameters. Consequently, the quality of the final best fit and the precision of the final physical parameters are fully determined by the density of the grid. This underlines, again, the necessity of a grid which is as dense as possible, allowing for interpolation. On the other hand, the grid-method has a plus-point: it is fast. Whereas the analysis with, e.g., a genetic algorithm approach (Mokiem et al. 2005, e.g.) needs parallel processors and several days of CPU to treat one target star, our grid-method will, on average, require less than half an hour on *one* computer, because no additional model computations are required.

2.2. The code AnalyseBstar

Our grid-based code, called AnalyseBstar, was developed for the spectroscopic analysis of B stars with winds. It is written in the Interactive Data Language (IDL), which allows for interactive manipulation and visualization of data. It fully relies on the extensive grid of NLTE model atmospheres and the emerging line profiles presented in Lefever et al. (2007a, see also `Appendix B.8` for a brief overview of the considered parameter set) and is developed to treat large samples of stars in a homogeneous way. We use continuum normalized H, He and Si lines to derive the photospheric properties of the star and the characteristics of its wind. Such an automated method is

[2] 180 CPU months were needed to compute the full grid of almost 265 000 models. To reduce the effective computation time, calculations were done on a dedicated Linux cluster of 5 dual-core, dual-processor computers (3800 MHz processors, sharing 4 Gb RAM memory and 8 Gb swap memory), amounting to 20 dedicated CPU processors, in addition to 40 more regularly used institute CPUs (8 of 3800MHz and 32 of 3400MHz). The grid filled 60% of a terabyte disk, connected to a Solaris 10 host pc.

not only homogeneous, but also objective and robust. A full description of the design of AnalyseBstar, including the preparation of the input, the iteration cycle for the determination of each physical parameter and the inherent assumptions, is given in Appendix B[3].

The intrinsic nature of our procedure allows us to derive estimates for the 'real' parameters of the star, which in most cases are located in between two model grid points. In what follows, we refer to them as 'interpolated values'. The corresponding grid values are the parameters corresponding to the grid model lying closest to these interpolated values.

Furthermore, we will denote the surface gravity as derived from fitting the Balmer line wings as $\log g$, while the gravity corrected for centrifugal terms (required, e.g., to estimate consistent masses) will be denoted by $\log g_c$. The (approximate) correction itself is obtained by adding the term $(v \sin i)^2/R_*$ to the uncorrected gravity (Repolust et al. 2005, and references therein).

2.3. Testing the method

2.3.1. Convergence tests for synthetic FASTWIND spectra

Before applying AnalyseBstar to observed stellar spectra, we tested whether the method was able to recover the parameters of synthetic FASTWIND input spectra. To this end, we created several synthetic datasets in various regions of parameter space, with properties representative for a 'typical' GAUDI spectrum. For more details on the setup of this test dataset and the results of the convergence tests, we refer to Appendix A. In all cases, the input parameters were well recovered and no convergence problems were encountered. Minor deviations from the input parameters were as expected and within the error bars. Also the derived $v \sin i$ -values, which are difficult to disentangle from potential macroturbulent velocities, agreed very well with the inserted values, irrespective of $v_{\rm macro}$. This shows that the Fourier Transform method of Gray (1973, 1975), whose implementation by Simón-Díaz & Herrero (2007) we used, indeed allows to separate both effects (but see below). All together, this gave us enough confidence to believe that our procedure will also be able to recover the physical parameters from real spectral data.

2.3.2. FASTWIND vs. Tlusty: profile comparison and analysis of Tlusty spectra

As an additional test, we compared line profiles based on FASTWIND models with negligible mass loss with their corresponding counterpart in the grid computed with the NLTE model atmosphere code Tlusty (Hubeny & Lanz 2000), which allows for a fully consistent NLTE metal line blanketing as well. This resulted in an overall good agreement, except for low gravity stars, where differences arise. It concerns differences in the forbidden He I components (which are quire strong in FASTWIND, but almost absent in Tlusty), the Balmer line wings (which are a bit stronger in FASTWIND than in Tlusty, yielding slightly lower $\log g$ values) and the Si II/III EW ratio for $T_{\rm eff} > 18$ kK (which is larger for FASTWIND than for Tlusty - due to both stronger Si II and weaker Si III lines -, yielding higher $T_{\rm eff}$ values). The reason that FASTWIND predicts stronger Balmer line wings is due to differences in the broadening functions and an underestimated photospheric line pressure, which can affect the photospheric structure of low-gravity objects. Differences are about or below 0.1 dex, and become negligible for dwarf stars. Except for the problem with the forbidden components, the profiles of the cooler models ($T_{\rm eff} < 18$ kK) compare very well.

To check the uncertainty in the synthetic profiles, we applied AnalyseBstar to profiles of six prototypical Tlusty models at 3 different temperature points (15 000, 20 000, and 25 000 K) and at a high and a low gravity. We added artificial noise to the data and artificially broadened the profiles with a fixed projected rotational velocity. The results of the comparison can be found in Table 1. The input and output fundamental parameters agree very well within the resulting errors, with only one exception, being the model with the high $T_{\rm eff}$ and higher $\log g$, where the temperature is off by 2 000 K.

Around 20kK, we experience similar difficulties to retrieve a unique temperature as in the cool B star domain, i.e. depending on the gravity, we may have only one stage of Si available, in this case Si III. Indeed, whereas the Si II lines are clearly visible in the higher gravity test case ($\log g$ = 3.00), they are no longer detectable in the lower gravity case ($\log g$ = 2.25). At this $T_{\rm eff}$, there are (unfortunately) no obvious Si IV lines yet, which complicates the analysis. Even though, AnalyseBstar is still able to retrieve the correct effective temperature, albeit with somewhat larger errors, using the same alternative method as for late B type stars when there is only Si II available (see 'method 2' in Section B.3).

Table 1. Result of applying AnalyseBstar to synthetic Tlusty profiles, which are artificially adapted to obtain a typical SNR of 150 and a projected rotational broadening of $v \sin i = 50$ km s^{-1}. $T_{\rm eff,in}$ and $\log g_{\rm ,in}$ are, respectively, the input effective temperature and gravity of the Tlusty spectra. $T_{\rm eff,out}$ and $\log g_{\rm ,out}$ represent the best matching ($T_{\rm eff}$, $\log g$)-combination in the FASTWIND grid.

$T_{\rm eff,in}$ (kK)	$\log g_{\rm ,in}$ (cgs)	$T_{\rm eff,out} \pm \Delta$ (kK)	$\log g_{\rm ,out} \pm \Delta$ (cgs)
15	1.75	15.0 ± 0.5	1.7 ± 0.05
15	3.00	15.5 ± 0.5	3.0 ± 0.10
20	2.25	20.0 ± 1.0	2.2 ± 0.10
20	3.00	21.0 ± 1.0	3.2 ± 0.20
25	2.75	25.0 ± 1.0	2.7 ± 0.05
25	3.00	27.0 ± 1.0	3.1 ± 0.10

[3] Manual available upon request from the authors.

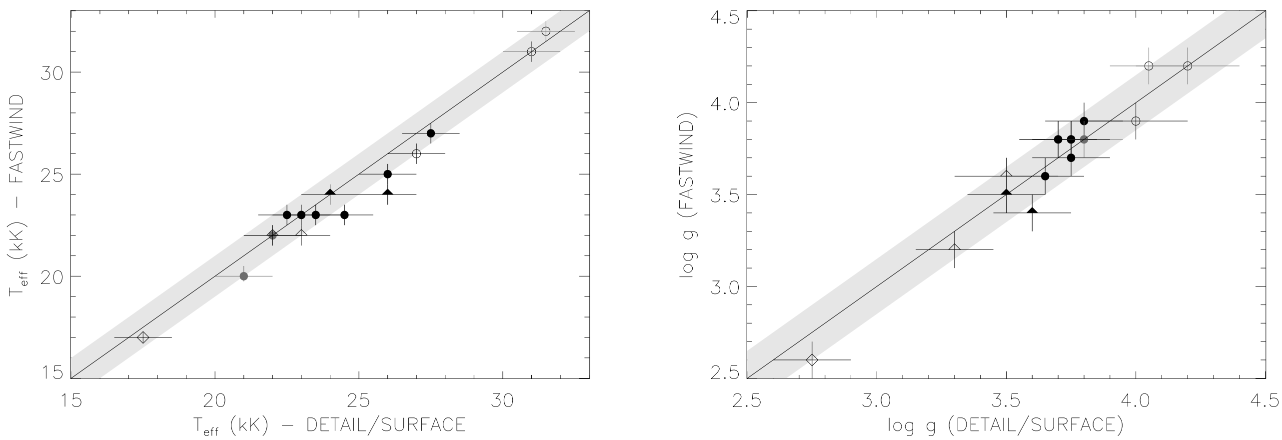

Figure 1. Comparison of the effective temperatures (left) and surface gravities (right) derived with FASTWIND (AnalyseBstar) with those found by Morel et al. (2006, 2008) and Briquet & Morel (2007) using DETAIL/SURFACE, for the β Cephei stars (black), SPBs (grey) and some well-studied hot B stars (open symbols). Supergiants are indicated as diamonds, giants as triangles and dwarfs as circles. The shaded area around the one-to-one relation (straight line) denotes the uncertainty on the derived fundamental parameters of Morel et al. (2006, 2008) and Briquet & Morel (2007) (i.e., 1 000 K in $T_{\rm eff}$ and 0.15 in $\log g$).

2.3.3. Comparison with fit-by-eye results for well-studied pulsators

Having thoroughly tested that AnalyseBstar indeed converges towards the optimum solution and that it is able to recover the input parameters of synthetic spectra, we performed an additional test on real spectra. We tested our method on a selected sample of high-quality, high-resolution spectra of pulsating B stars (β Cephei and Slowly Pulsating B stars (SPB)). The (mean) spectra of these stars have a very high SNR, attained through the addition of a large number of individual exposures (see, Morel et al. 2007). Given that we excluded binaries from our GAUDI sample (see Section 3.1), we also ignored θ Oph and β Cru for the test sample. Moreover, V2052 Oph is chemically peculiar and was thus excluded, as well as V836 Cen for which only one spectrum is available. Thus we limited our test sample to those single stars in Morel et al. (2007) for which numerous high-quality spectra were available. Because of the high quality of these spectral time series, they are ideally suited for testing AnalyseBstar.

The β Cephei stars and two of the SPB stars were analyzed in detail by Morel et al. (2006, 2008) and Briquet & Morel (2007), respectively. These authors used the latest version of the NLTE line formation codes DETAIL and SURFACE (Giddings 1981; Butler & Giddings 1985), in combination with plane-parallel, fully line-blanketed LTE Kurucz atmospheric models (ATLAS9, Kurucz 1993), to determine (by eye) the atmospheric parameters and element abundances of low-luminosity class objects with negligible winds. The outcome of the comparison with their results are summarized in Tables 2a to 2c, and in Figs. 1 and 2. Although the effective temperatures derived from FASTWIND tend to be, on the average, slightly below the ones derived from DETAIL/SURFACE, it is clear that, within the error bars, FASTWIND and DETAIL/SURFACE give consistent results for $T_{\rm eff}$ and $\log g$ (Fig. 1) as well as for log n(Si)/n(H) (Fig. 2),

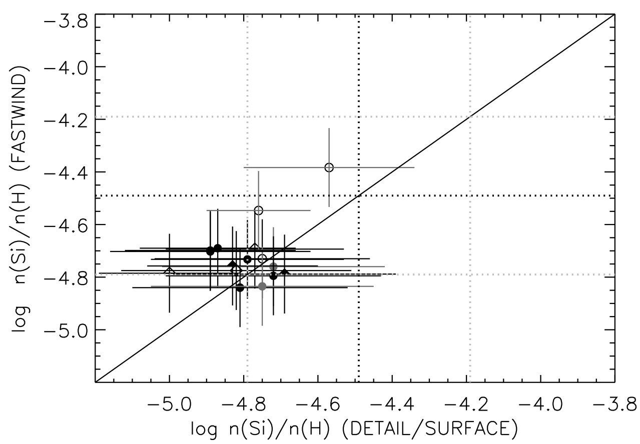

Figure 2. Comparison between the Si abundances derived from AnalyseBstar and those derived from DETAIL/SURFACE for the set of photometric targets, used to evaluate the performance of AnalyseBstar. The black dotted lines represent the solar Si abundance (log n(Si)/n(H) = -4.49), while the grey dotted lines represent a depletion and enhancement of Si by 0.3 dex (i.e., -4.79 and -4.19, respectively). Symbols have the same meaning as in Fig. 1. Individual error bars are indicated.

On the other hand, the $v \sin i$ values derived by Morel et al. (2008) are typically slightly above those derived by us. This is readily understood as their values implicitly include the macroturbulent velocity, which has not been taken into account as a separate broadening component. In those cases where we derive a vanishing $v_{\rm macro}$, the $v \sin i$ values are in perfect agreement. Aerts et al. (2009) recently suggested that macroturbulence might be explained in terms of collective pulsational velocity broadening due to the superposition of a multitude

Table 2a. Fundamental parameters of well-studied β Cephei stars (spectral types from SIMBAD), as derived from AnalyseBstar: the effective temperature ($T_{\rm eff}$), the surface gravity ($\log g$, not corrected for centrifugal acceleration due to stellar rotation), the helium abundance (n(He)/n(H), with solar value 0.10), the Si abundance (log n(Si)/n(H), with solar value -4.49), the microturbulence (ξ), the projected rotational velocity ($v \sin i$) and the macroturbulent velocity ($v_{\rm macro}$). We list the values of the closest grid model, except for the Si abundance, where the interpolated value is given. In italics, we display the results from the DETAIL/SURFACE analysis by Morel et al. (2006, 2008). For 12 Lac, we additionally list the parameters which we retrieve when forcing $v_{\rm macro}$ to be zero while keeping the value for $v \sin i$ (indicated between brackets, see text for details). All stars have thin or negligible winds.
Typical errors for $T_{\rm eff}$ and $\log g$ are, respectively, 1 000 K and 0.15 for the comparison data sets of Morel et al. (2006, 2008) and Briquet & Morel (2007), which is somewhat more conservative than the errors adopted in this study. We adopt typical 1-σ errors of 0.10 dex for $\log g$, 1 000 K for $T_{\rm eff} > 20\,000\ K$ and $T_{\rm eff} < 15\,000\ K$, and 500 K for $15\,000\ K \leq T_{\rm eff} \leq 20\,000\ K$. The error for the derived Si-abundance, log n(Si)/n(H), has been estimated as 0.15 and 0.20 dex for objects above and below 15 000 K, respectively (see also Section B.3.)

HD number	alternative name	Spectral Type	$T_{\rm eff}$ (K)	$\log g$ (cgs)	n(He)/n(H)	log n(Si)/n(H)	ξ (km s^{-1})	$v \sin i$ (km s^{-1})	$v_{\rm macro}$ (km s^{-1})
46328	ξ^1 CMa	B0.5-B1IV	27000	3.80	0.10	-4.69	6	9 ± 2	11
			27500	*3.75*		*-4.87 ± 0.21*	*6 ± 2*	*10 ± 2*	-
50707	15 CMa	B1III	24000	3.40	0.10	-4.79	12	34 ± 4	38
			26000	*3.60*		*-4.69 ± 0.30*	*7 ± 3*	*45 ± 3*	-
205 021	β Cep	B1IV	25000	3.80	0.10	-4.70	6	26 ± 3	24
			26000	*3.70*		*-4.89 ± 0.23*	*6 ± 3*	*29 ± 2*	-
44743	β CMa	B1.5III	24000	3.50	0.10	-4.76	15	19 ± 4	20
			24000	*3.50*		*-4.83 ± 0.23*	*14 ±3*	*23 ± 2*	-
214 993	12 Lac	B1.5IV	23000	3.60	0.10	-4.41	6	44 ± 6	37
						[-4.83]	[12]		[0]
			24500	*3.65*		*-4.89 ± 0.27*	*10 ± 4*	*42 ± 4*	-
16582	δ Ceti	B1.5-B2IV	23000	3.90	0.10	-4.80	6	14 ± 2	0
			23000	*3.80*		*-4.72 ± 0.29*	*1^{+3}_{-1}*	*14 ± 1*	-
886	γ Peg	B1.5-B2IV	23000	3.80	0.10	-4.84	< 3	10 ± 1	0
			22500	*3.75*		*-4.81 ± 0.29*	*1^{+2}_{-1}*	*10 ± 1*	-
29248	ν Eri	B1.5-B2IV	23000	3.70	0.10	-4.73	10	21 ± 3	39
			23500	*3.75*		*-4.79 ± 0.26*	*10 ± 4*	*36 ± 3*	-

Table 2b. Same as for Table 2a, but now for some well-studied SPBs. In italics, we show the results of the DETAIL/SURFACE analysis by Briquet & Morel (2007).

HD number	alternative name	Spectral Type	$T_{\rm eff}$ (K)	$\log g$ (cgs)	n(He)/n(H)	log n(Si)/n(H)	ξ (km s^{-1})	$v \sin i$ (km s^{-1})	$v_{\rm macro}$ (km s^{-1})
3360	ζ Cas	B2IV	22000	3.80	0.10	-4.76	< 3	18 ± 2	13
			22000	*3.70*		*-4.72 ± 0.30*	*1 ± 1*	*19 ± 1*	-
85953	V335 Vel	B2IV	20000	3.80	0.10	-4.84	6	30 ± 1	20
			21000	*3.80*		*-4.75 ± 0.30*	*1 ± 1*	*29 ± 2*	-
3379	53 Psc	B2.5IV	20000	4.30	0.10	-4.73	< 3	48 ± 8	43
74195	o Vel	B3IV	16500	3.70	0.10	-4.79	< 3	18 ± 2	18
160762	ι Her	B3IV	19500	4.10	0.10	-4.86	3	8± 2	0
25558	40 Tau	B3V	17500	4.00	0.10	-4.72	6	28 ± 2	31
181558	HR 7339	B5III	15000	4.00	0.10	-4.79	6	17 ± 2	0
26326	HR 1288	B5IV	15500	3.60	0.10	-4.49	< 3	17 ± 1	17
206540	HR 8292	B5IV	13500	3.80	0.10	-4.79	3	15 ± 2	0
24587	HR 1213	B5V	14500	4.00	0.10	-4.79	< 3	25 ± 4	21
28114	HR 1397	B6IV	14000	3.50	0.10	-4.79	< 3	21 ± 4	17
138764	HR 5780	B6IV	14500	3.90	0.10	-4.51	3	21 ± 2	0
215573	HR 8663	B6IV	13500	3.80	0.10	-4.49	< 3	8 ± 1	0
39844	HR 2064	B6V	14500	3.70	0.10	-4.39	< 3	16 ± 1	0
191295	V1473 Aql	B7III	13000	3.70	0.10	-4.79	3	16 ± 1	15
21071	V576 Per	B7V	13500	3.70	0.10	-4.79	3	22 ± 1	0
37151	V1179 Ori	B8V	12500	3.80	0.10	-4.79	< 3	20 ±2	0

Table 2c. Same as for Table 2a, but now for some well-studied hot B stars. In italics, we display the independent results from the DETAIL/SURFACE analysis by Morel et al. (2006, 2008), except for θ Car and τ Sco which can be found in Hubrig et al. (2008). For τ Sco, we additionally compare with the values found by Mokiem et al. (2005) using a genetic algorithm approach (superscript *M*). The results for two objects overlapping with the study of Przybilla et al. (2008) are also indicated (superscript *P*).

HD number	alternative name	Spectral Type	$T_{\rm eff}$ (K)	$\log g$ (cgs)	n(He)/n(H)	log n(Si)/n(H)	ξ (km s^{-1})	$v \sin i$ (km s^{-1})	$v_{\rm macro}$ (km s^{-1})
93030	θ Car	B0Vp	31000	4.20	0.15	-4.38	10	108 ± 3	0
			31000	*4.20*	-	*-4.57 ± 0.23*	*12 ± 4*	*113 ± 8*	-
149 438	τ Sco	B0.2V	32000	4.20	0.10	-4.55	6	10 ± 2	0
			31500	*4.05*	-	*-4.76 ± 0.14*	*2 ± 2*	*8 ± 2*	-
			31900^M	*4.15^M*	*0.12^M*	-	*10.8^M*	*5^M*	-
			32000^P	*4.30^P*	*0.10^P*	*-4.50^P*	*5^P*	*4^P*	*4^P*
36591	HR 1861	B1V	26000	3.90	0.10	-4.73	6	13 ± 1	0
			27000	*4.00*	-	*-4.75 ± 0.29*	*3 ± 2*	*16 ± 2*	-
			27000^P	*4.12^P*	*0.10^P*	*-4.52^P*	*3^P*	*12^P*	-
52089	ϵ CMa	B1.5-B2II/III	22000	3.20	0.10	-4.69	15	32 ± 2	20
			23000	*3.30*	-	*-4.77 ± 0.24*	*16 ± 4*	*28 ± 2*	-
35468	γ Ori	B2II-III	22000	3.60	0.10	-4.79	10	46 ± 8	37
			22000	*3.50*	-	*-5.00 ± 0.19*	*13 ± 5*	*51 ± 4*	-
51309	ι CMa	B2.5Ib-II	17000	2.60	0.10	-4.78	15	27 ± 4	39
			17500	*2.75*	-	*-4.82 ± 0.31*	*15 ± 5*	*32 ± 3*	-

of gravity modes with low amplitudes (see also `Appendix B.4`). In this respect, we expect stars for which $v_{\rm macro}$ differs from zero to be pulsators.

For few overlapping objects, we could also compare our results with those from independent studies by Mokiem et al. (2005), based on FASTWIND predictions for H and He lines and using a genetic algorithm approach, and by Przybilla et al. (2008), using ATLAS9/DETAIL/SURFACE, allowing for a comparison of H, He, and Si. The consistency with both studies is quite good, except for the Si abundance of HD 36591 as determined by Przybilla et al. For this object, Hubrig et al. (2008) have obtained a value close to ours, using the same ATLAS9/DETAIL/SURFACE code. Ad hoc, we cannot judge the origin of this discrepancy.

For two targets, HD 85953 and τ Sco, somewhat larger differences in the derived microturbulence are found. For HD 85953, this difference is compensated by an opposite difference in the derived Si abundance. For τ Sco, on the other hand, the derived microturbulence (and also the Si abundance) is in perfect agreement with the values provided by Hubrig et al. (2008) and Przybilla et al. (2008) within the defined error bars, whereas the value for the microturbulence derived by Mokiem et al. (2005) differs substantially. As they did not derive the Si abundance, we cannot judge on the difference in Si abundance this would have caused.

An even more detailed test can be done for stars with seismically determined values of the fundamental parameters. 12 Lac is such a star. It is known as a non-radial pulsator with at least 11 independent oscillation frequencies (Handler et al. 2006). The fact that 12 Lac is a rich pulsator clearly shows up in the line profiles, which are strongly asymmetric. Especially the Si III triplets (Si III 4552-4567-4574 and Si III 4813-4819-4829) are skew. Fig. 3 shows the observed spectrum (black), which is a combination of 31 exposures. Using the Fourier Transform method, we find the projected rotational velocity to be 44 km s^{-1}, which is slightly above the 36 km s^{-1} derived from modelling the line profile variations (Desmet et al. 2009). Including macroturbulence in the spectral line fitting, results in the following parameters: $T_{\rm eff}$ = 23 000 K ± 1 000 K, $\log g$ = 3.6 ± 0.1, ξ = 6 ± 3 km s^{-1}, solar He and Si abundances (solid grey lines in Fig. 3). Actually, the derived surface gravity is in perfect agreement with the seismically determined value of $\log g$ (3.64-3.70) determined by Desmet et al. (2009).

Except for the Si abundance, our results are also in agreement with Morel et al. (2006, see Table 2a), who derived $T_{\rm eff}$ = 24 500 K ± 1 000 K, $\log g$ = 3.65 ± 0.15, ξ = 10 ± 4 km s^{-1} and depleted Si abundances as seem to be typical for B dwarfs in the solar neighborhood. To account for the pulsational broadening, we needed to include a macroturbulence of 37 km s^{-1}. Forcing the macroturbulence to be zero while keeping the derived value of $v \sin i$ leaves the main physical parameters ($T_{\rm eff}$, $\log g$ and He abundance) unaltered, while the microturbulent velocity and the Si abundance change to compensate for the change in profile shape: the microturbulence becomes larger (12 km s^{-1}, broader lines) and the Si abundance becomes lower (depleted, log n(Si)/n(H) ≈ -4.83). As expected, this depleted Si abundance *is* in agreement with Morel et al. (2006), who did not include $v_{\rm macro}$ in their analysis. When evaluating the fit quality, we find, besides the expected mismatch in the Si line wings, also a discrepancy in the line cores of He (dashed grey lines in Fig. 3). Following Aerts et al. (2009), this might be improved by accounting for the pulsational broadening introduced by the collective set of detected oscillations in 12 Lac, as this would result in a shape intermediate between a rotation and a Gaussian profile. However, the only way one can account for this, is by using an appropriate time series of spectra. The above example illustrates that we need to account for pulsational broadening to correctly assess the Si abundance and microturbulence. In this sense, it is advisable to work with '$v_{\rm macro}$' as a substitute for the time-dependent broadening in the case of 'snapshot' spectra.

3. Application to the GAUDI B star sample

3.1. CoRoT & GAUDI

The French-led European space mission CoRoT (Convection, Rotation, and planetary Transits; see "the CoRoT Book", Fridlund et al. 2006) was launched successfully on December 27th, 2006. The observational setup of the CoRoT seismology programme (observations of a small number of bright stars over a very long period) made target selection a crucial issue. Due to the acute shortage of available information on the potential CoRoT targets, the need for additional data was high. Therefore, an ambitious ground-based observing program for more than 1500 objects was set up, under the leadership of C. Catala at Meudon, to obtain Strömgren photometry (*uvbyβ*) as well as high-resolution spectroscopy (FEROS, ELODIE, SARG, CORALIE, GIRAFFE, coudé spectrograph at the 2m telescope in Tautenburg, CATANIA). These data were collected in an extensive catalogue, maintained at LAEFF (Laboratorio de Astrofísica Espacial y Física Fundamental) and baptized *GAUDI*: Ground-based Asteroseismology Uniform Database Interface (Solano et al. 2005).

The Be stars within the GAUDI database were studied by Frémat et al. (2006) and Neiner et al. (2005) and are omitted here, since the FASTWIND code is not developed to treat stars with a circumstellar disc. Also double-lined spectroscopic binaries (SB2) were omitted from our sample, as their combined spectra make an accurate fundamental parameter estimation impossible as long as their flux ratios are not known. Among the GAUDI sample, we discovered a few candidate spectroscopic binaries, which were not known to be SB2s. It concerns HD 173003 (B5), HD 181474 (B5), HD 42959 (B8), HD 50982 (B8, variable star), HD 51150 (B8, clearly asymmetric profiles), HD 181761 (B8), HD 45953 (B9, variable star) and HD 46165 (B9).

For the few available SARG data, only the default normalized spectra were inserted into the database and we failed to get hands on the raw data, which would be needed for a careful rerectification. Indeed, the poor continuum rectification is especially clear from Hβ, but also shows up in other line profiles. Moreover, the spectral coverage of the SARG spectra is too small to deduce any useful information. Therefore, we excluded all SARG spectra from our sample. The same accounts for the CATANIA spectra, for which the spectral quality was too poor for a detailed spectral analysis, so also these spectra were omitted. We thus restrict this paper to FEROS and ELODIE spectra, having a resolution of 48 000 and 50 000, respectively.

The standard FITS data of the FEROS and ELODIE spectra in the GAUDI database contain information about both the normalized spectrum, resulting from the pipeline reduction, and the unnormalized spectrum. Since the quality of normalization turned out to be insufficient for our detailed analyses, one of us (TM) redid the normalization for all spectral ranges around the diagnostic lines in a uniform way using IRAF[4] to ensure a homogeneous treatment of the sample.

Among the GAUDI sample, we find, as expected, a lot of fast rotators. Their spectra usually contain insufficient line information due to their high projected rotational velocities. Often, only the Balmer lines and the strongest He I lines (i.e. He I 4026, 4471 and 4922) can be detected, while all Si lines are lost. The stars that were discarded for this reason are HD 182519 (B5, >300 km s^{-1}), HD 50751 (B8, >200 km s^{-1}), HD 56006 (B8, >150 km s^{-1}), HD 45515 (B8 V, >190 km s^{-1}), HD 182786 (B8, >160 km s^{-1}), HD 50252 (B9 V, >140 km s^{-1}), HD 169225 (B9, >160 km s^{-1}), HD 171931 (B9, >250 km s^{-1}), HD 174836 (B9, >140 km s^{-1}), 176258 (B9 V, >160 km s^{-1}), HD 179124 (B9 V, >270 km s^{-1}), and HD 45760 (B9.5 V, >190 km s^{-1}). For some of the GAUDI stars, we were able to fit the spectrum despite the high projected rotational velocity, but their resulting parameters cannot be very reliable. This concerns HD 51507 (B3 V, 148 km s^{-1}), HD 45418 (B5, 237 km s^{-1}), HD 46487 (B5 Vn, 265 km s^{-1}), HD 178744 (B5 Vn, 224 km s^{-1}), HD 43461 (B6 V, 210 km s^{-1}), HD 44720 (B8, 160 km s^{-1}), HD 49643 (B8 IIIn, 296 km s^{-1}), HD 173370 (B9V, 282 km s^{-1}, double-peaked Hα profile), HD 179124 (B9 V, 278 km s^{-1}), and HD 181690 (B9 V, 189 km s^{-1}). Their parameters can be found in Table 3.

For other targets, we have only spectra of insufficient quality available which cannot be used for spectral line fitting purposes. It concerns HD 48691 (B0.5 IV), HD 168797 (B3 Ve), HD 178129 (B3 Ia), HD 57608 (B8 III, possible instrumental problem), HD 44654 (B9), HD 45257 (B9), and HD 53204 (B9).

For a few stars, we have both an ELODIE and a FEROS spectrum available, e.g., for HD 174069. From inspection of the spectra, it was immediately clear that there are differences in the line profiles, in particular the wings of the Balmer lines are much less pronounced in the ELODIE spectra (see Fig. 4). Also other stars, for which we have both a FEROS and an ELODIE spectrum available, show the same discrepancy, so there seems to be a systematic effect. We fitted both spectra and came up with a different set of parameters. The difference in $\log g$ is large (> 0.5 dex) and certainly worrisome. To investigate this problem, we looked up the spectra in the FEROS and ELODIE archives and realized that the merging of the ELODIE spectra by the pipeline is far less accurate than for the FEROS spectra. This is due to an inaccurate correction for the blaze function in the case of the ELODIE pipeline. Due to this, we also redid the merging of the orders for the ELODIE spectra, before the normalization. This led to a much better agreement with the available FEROS spectra. We thus advise future users against working with the merged and normalized spectra from GAUDI, but rather to go back to the original spectra in the FEROS and ELODIE archives, and not only redo the normalization but even the merging in the case of the ELODIE spectra. Unfortunately, not all stars had a spectrum

[4] IRAF (Image Reduction and Analysis Facility) is distributed by the National Optical Astronomy Observatories, operated by the Association of Universities for Research in Astronomy, Inc., under cooperative agreement with the National Science Foundation, USA.

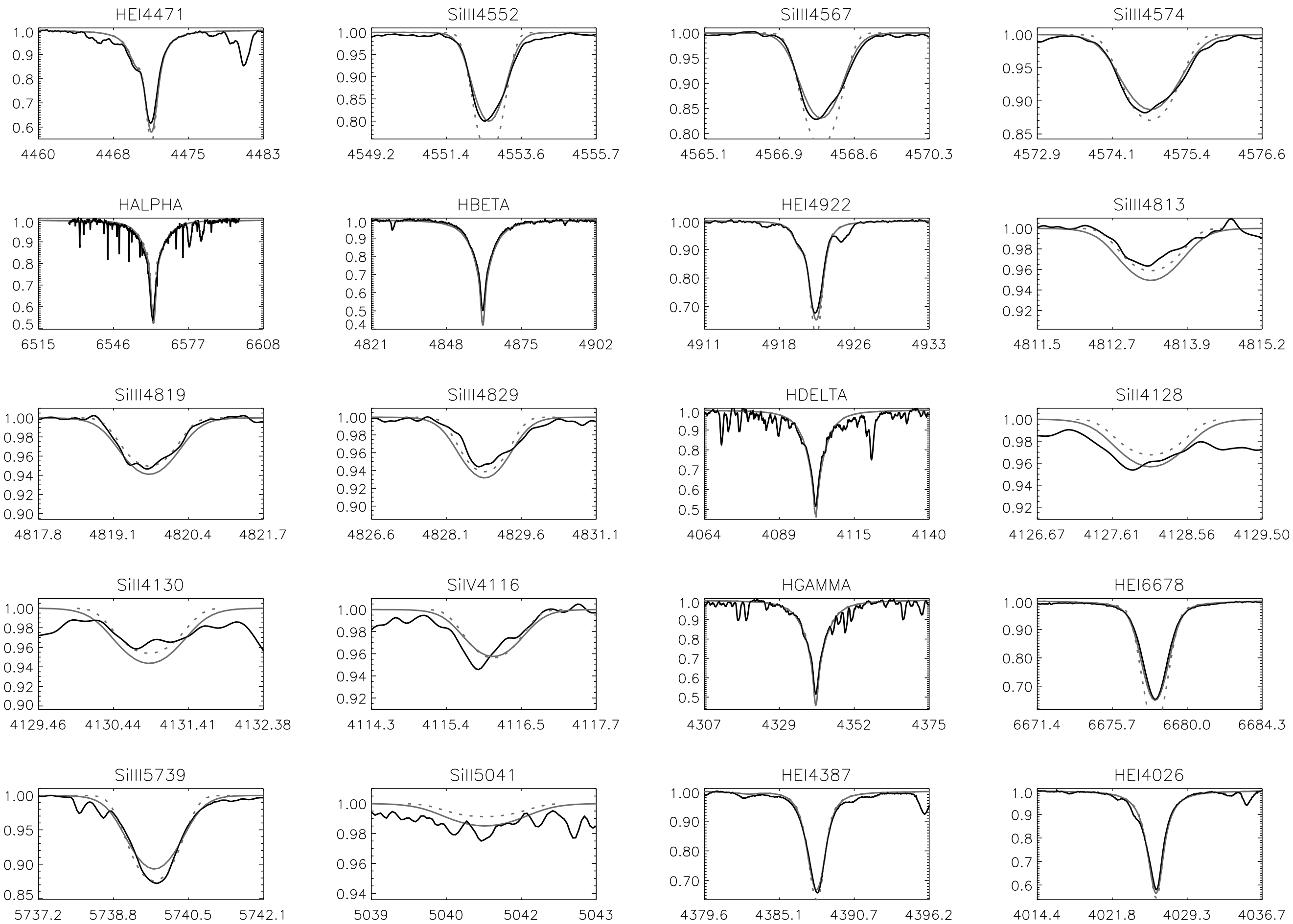

Figure 3. Illustration of the effects of time-independent broadening on the derived parameters for 12 Lac (B2 III). The observed line profiles (solid black lines) are fitted using AnalyseBstar. Inclusion of time-independent broadening (by means of macroturbulence) yields the solid grey fit, with optimum values of $v \sin i = 44\,\mathrm{km\,s^{-1}}$ and $v_{\mathrm{macro}} = 37\,\mathrm{km\,s^{-1}}$. Forcing the macroturbulence to be zero leaves all parameters but the Si abundance and the microturbulence unaltered. The resulting fit is represented by the grey dashed lines.

available in the ELODIE archives though, e.g., for HD 47887 (B2 III), HD 52559 (B2 IV-V), HD 48977 (B2.5 V), HD 50228 (B5), HD 57291 (B5), HD 51892 (B7 III), HD 52206 (B8) and HD 53202 (B9), we could not find the original spectrum, so we left out these stars from our analysis. For HD 43317 (B3 IV), the archival spectrum was not usable.

Finally, for 17 of the remaining stars, we could not find a satisfactory fit, and we decided to leave them out of the sample. One possible explanation might be that they are single-lined binaries (see also Massey et al. 2009 who encountered similar problems when analyzing a large sample of LMC/SMC O-stars).

All together, this, unfortunately, reduces our sample a lot, and we are only left with a bit more than a third of the targets initially in the database: 66 out of 187 objects. Moreover, most of the objects are late B-type stars. Fig. 5 shows a histogram with the breakdown of the sample following spectral subtype. The ratio marked above each bin indicates the number of analyzed targets compared to the total amount that was available before the selection procedure.

3.2. Analysis results

3.2.1. Example fits

To illustrate the obtained quality of the final fits, we show in Figs. 6 to 8 some examples of the resulting spectral fits for three very different stars included in GAUDI: a ‘cool’ giant, a hot supergiant and a middle type dwarf.

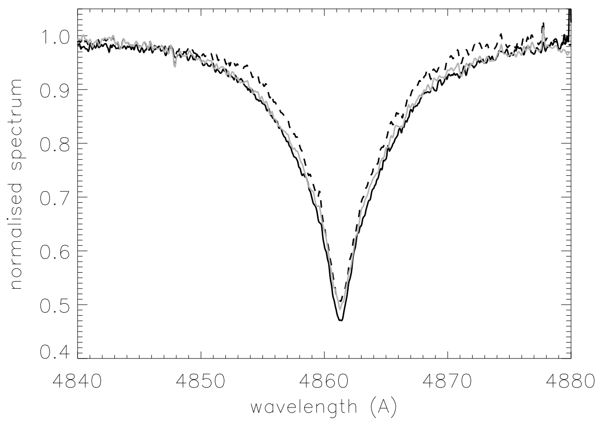

Figure 4. HD 174069: Significant (and apparently systematic) discrepancies are observed between the line profiles of the FEROS (solid black line) and the ELODIE (dashed black line) spectrum from the GAUDI database. This leads to considerable discrepancies in the derived stellar parameters. In grey, we show the normalized ELODIE spectrum obtained from the ELODIE archives, which shows a much better agreement with the available FEROS spectra.

Table 3: Stellar parameters of the analyzed GAUDI B type stars. The first two columns give the HD number of the star and the spectral type (SpT) taken from SIMBAD. Then we list the effective temperature ($T_{\rm eff}$) of the model which was found by AnalyseBstar to match the observations best, the surface gravity corrected for centrifugal acceleration ($\log g_c$, with corresponding uncertainty $\Delta\log g$), the He abundance (n(He)/n(H), where 0.10 is solar), the interpolated Si abundance when available, otherwise the closest grid Si abundance (log n(Si)/n(H), where -4.49 is solar, -4.19 is enhanced and -4.79 is depleted) and the microturbulence (ξ); $v\sin i$ is the projected rotational velocity as obtained by applying the implementation of the Fourier Transform method of Gray (1973, 1975) by Simón-Díaz & Herrero (2007). In some cases, we need an additional broadening to explain the line profiles. Therefore, we list the required macroturbulent velocity ($v_{\rm macro}$) and indicate the stars for which we suspect they might be pulsators from the fact that they have a significant $v_{\rm macro}$. We attribute a flag to each star, to represent the obtained fit quality or problems we encountered during the fitting procedure: 1 - well-fitted, 2 - probably a wrong spectral type (about 1 000 K or more away from the calibrations, proposed spectral type indicated in the 'remarks'-column), 3 - no or hardly any Si lines available, mostly due to fast rotation, 4 - not very reliable fit (for other reasons than fast rotation, see 'remarks'), 5 - He weak/Si strong, 6 - fitting of Hα, Hβ, and Hγ line profiles complicated due to very broad wings which abruptly change into very narrow line cores ($\log g$ may be less accurate). In the last column, a few additional comments are given. The formal uncertainty on the effective temperature is 1,000 K for $T_{\rm eff} > 20,000$ K and $T_{\rm eff} < 15\,000\ K$, and 500 K for $T_{\rm eff} < 15,000\ K \leq T_{\rm eff} \leq 20\,000\ K$. The formal uncertainty on the microturbulence and on the He and Si abundance is half of the grid step in most cases: 2 km s^{-1} and 0.025 dex, respectively. For objects below 15 000 K we adopt somewhat largers errors (3-σ deviation corresponding to 2 grid steps): 3 km s^{-1}, 0.033 and 0.2 dex, respectively.

HD number	SpT	$T_{\rm eff}$ (K)	$\log g_c$ (cgs)	n(He)/n(H)	log n(Si)/n(H)	ξ (km s^{-1})	$v\sin i$ (km s^{-1})	$v_{\rm macro}$ (km s^{-1})	suspected pulsator	flag	remarks
48434	B0III	28000	3.11 ± 0.10	0.10	-4.44	15	62 ± 3	31	yes	4	ELODIE, poor quality spectrum, He lines too strong Balmer lines not well fitted due to bumps in blue wings
52382	B1Ib	23000	2.71 ± 0.10	0.15	-4.67	20	56 ± 5	53	yes	4	P Cygni profile Hα not reproduced, Hβ and Hγ not well fitted
170580	B2V	20000	4.10 ± 0.10	0.10	-4.81	6	11 ± 1	0	no	1	N(He)/N(H) lower than solar
44700	B3V	17500	3.80 ± 0.10	0.10	-4.93	6	8 ± 1	0	no	1	N(He)/N(H) lower than solar
181074	B3	20000	3.64 ± 0.10	0.10	-4.35	12	133 ± 7	0	no	2	probably B2, fast rotator
45418	B5	16000	4.0 ± 0.20	0.10	-4.49	3	237 ± 28	0	no	3	
46487	B5Vn	14500	3.69 ± 0.10	0.15	-4.49	3	265 ± 5	0	no	3	
48215	B5V	14500	3.82 ± 0.10	0.10	-4.49	3	98 ± 3	48	yes	1	only Si II
54596	B5	20000	3.31 ± 0.05	0.10	-4.48	6	69 ± 6	53	yes	2	only Si III, probably B2
58973	B5	15000	3.43 ± 0.20	0.10	-4.49	3	94 ± 1	50	yes	1	
177880	B5V	14500	3.81 ± 0.10	0.10	-4.49	3	49 ± 1	23	yes	1	
178744	B5Vn	14500	3.71 ± 0.20	0.10	-4.49	12	224 ± 5	0	no	3	
43461	B6V	13500	3.35 ± 0.10	0.10	-4.79	3	210 ± 5	0	no	3	
48807	B7Iab	12500	2.00 ± 0.10	0.10	-4.28	6	24 ± 1	27	yes	1	
51360	B7III	13500	3.12 ± 0.10	0.10	-3.93	3	73 ± 1	55	yes	1	very high Si abundance
42677	B8	11000	3.55 ± 0.20	0.10	-4.79	6	121 ± 14	104	yes	2	probably B9
44720	B8	14000	3.96 ± 0.10	0.10	-4.19	3	160 ± 5	0	no	2	probably B5 or B6
45153	B8	11000	3.66 ± 0.10	0.10	-4.49	3	142 ± 4	0	no	2	probably B9
45284	B8	15000	4.10 ± 0.10	0.10	-4.19	3	52 ± 5	42	yes	2	SPB with magnetic field, skew Si II lines, probably B5
45397	B8	11500	3.59 ± 0.10	0.20	-4.79	6	156 ± 12	0	no	3	
45515	B8V	11000	4.18 ± 0.10	0.15	-4.49	3	190 ± 5	0	no	2, 3	probably B9
46616	B8	17500	4.20 ± 0.50	0.10	-4.24	3	8 ± 1	7	yes	5	He-weak star
47964	B8III	11500	3.01 ± 0.20	0.10	-4.79	3	49 ± 1	44	yes	1	
48497	B8	14000	3.70 ± 0.10	0.10	-4.58	3	14 ± 1	13	yes	4, 6	N(He)/N(H) lower than solar
49481	B8	11000	2.70 ± 0.20	0.20	-4.79	3	9 ± 1	13	yes	2, 6	probably B9
49643	B8IIIn	14500	3.88 ± 0.10	0.10	-4.19	3	296 ± 2	13	no	3	
49886	B8	10000	3.30 ± 0.20	0.10	-4.79	6	8 ± 1	16	yes	4, 6	
49935	B8	12500	3.33 ± 0.20	0.10	-4.79	6	92 ± 9	72	yes	1	$\log g$ may be too low?
50251	B8V	11500	3.00 ± 0.20	0.10	-4.79	3	9 ± 1	17	yes	1	emission line around Si III 4813 and Si IV 4212
50513	B8	11500	4.04 ± 0.10	0.10	-4.79	6	112 ± 5	80	yes	1	
55793	B8	11000	3.05 ± 0.05	0.20	-4.79	3	101 ± 1	56	yes	2	probably B9, $\log g$ may be too low?
56446	B8III	11500	3.21 ± 0.20	0.20	-4.19	3	229 ± 32	13	no	3	
170795	B8	15500	4.01 ± 0.10	0.10	-4.49	3	79 ± 7	37	yes	2	probably B5
171247	B8IIIsp	10000	2.83 ± 0.10	0.10	-4.19	6	66 ± 2	20	yes	4	peculiar line behaviour
173673	B8	10000	2.90 ± 0.10	0.20	-4.49	3	25 ± 2	26	yes	4, 6	too low $\log g$?
179761	B8II-III	12500	3.30 ± 0.05	0.10	-4.49	3	17 ± 1	12	yes	1	
180760	B8	17000	4.05 ± 0.10	0.10	-4.49	6	167 ± 3	0	no	3	wrong spectral type?
44321	B9	11000	3.62 ± 0.05	0.10	-4.79	6	90 ± 3	30	yes	1	
44354	B9	13000	3.94 ± 0.05	0.15	-4.79	10	121 ± 5	72	yes	2	probably B7 or B8
45050	B9V	11500	3.86 ± 0.10	0.10	-4.79	10	140 ± 47	0	no	3	
45516	B9	13000	3.90 ± 0.10	0.10	-4.49	6	281 ± 55	12	no	3	
45657	B9	11000	4.24 ± 0.10	0.10	-4.79	3	153 ± 36	0	no	3	
45709	B9	11000	3.95 ± 0.30	0.20	-4.79	10	231 ± 24	10	no	3	
45975	B9	11000	3.51 ± 0.10	0.15	-4.79	3	54 ± 1	56	yes	1	$v_{\rm macro}$ too high
46138	B9	12000	3.93 ± 0.05	0.10	-4.19	3	100 ± 5	0	no	4	
46886	B9	11000	3.00 ± 0.10	0.10	-4.79	3	16 ± 3	23	yes	1	$\log g$ too low?
47278	B9	10000	3.60 ± 0.05	0.10	-4.79	3	31 ± 4	25	yes	2	rather A0
48808	B9	12000	3.21 ± 0.10	0.10	-4.79	3	47 ± 14	63	yes	1	$v_{\rm macro}$ too high, rather B8
48957	B9	12000	3.10 ± 0.10	0.10	-4.79	3	24 ± 2	23	yes	4	$T_{\rm eff}$ too low?, wrong spectral type?
49123	B9	10000	3.41 ± 0.05	0.10	-4.79	3	45 ± 2	0	no	2	rather A0
52312	B9III	11000	3.04 ± 0.05	0.20	-4.49	3	175 ± 5	0	no	3	
53004	B9	11000	3.91 ± 0.20	0.10	-4.79	6	51 ± 7	54	yes	1	
54761	B9	11500	3.11 ± 0.10	0.10	-4.79	6	53 ± 1	71	yes	1	Balmer line cores slightly refilled, $\log g$ too high?
54929	B9	10000	3.11 ± 0.10	0.10	-4.49	3	46 ± 1	107	yes	4	fast rotator, difficult to fit, too high $v_{\rm macro}$
56613	B9	13000	3.92 ± 0.20	0.10	-4.79	6	91 ± 7	36	yes	2	rather, B7 or B8
172850	B9	11000	3.62 ± 0.10	0.10	-4.49	3	77 ± 4	0	no	1	
173370	B9V	11500	3.46 ± 0.10	0.10	-4.79	15	282 ± 8	0	no	4	very fast rotator, no Si lines available,double-peaked Hα profile, Hβ refilled on both sides of the line core
173693	B9	10000	3.32 ± 0.10	0.10	-4.79	3	60 ± 1	22	yes	2	rather A0
174701	B9	12500	3.68 ± 0.10	0.15	-4.49	3	170 ± 2	10	no	3	
175640	B9III	10000	3.20 ± 0.10	0.15	-4.49	3	7 ± 1	10	yes	2	rather A0
176076	B9	10000	3.41 ± 0.10	0.10	-4.79	3	42 ± 2	0	no	2	rather A0
176158	B9	13500	3.64 ± 0.10	0.15	-4.79	3	121 ± 11	0	no	2	rather B8
179124	B9V	12000	3.45 ± 0.10	0.10	-4.49	15	277 ± 6	0	no	3	
181440	B9III	11500	3.61 ± 0.50	0.10	-4.49	3	55 ± 7	32	yes	1	
181690	B9V	13000	3.42 ± 0.10	0.10	-4.49	6	189 ± 5	0	no	3	
182198	B9V	11000	3.10 ± 0.10	0.10	-4.79	3	23 ± 1	12	yes	1	

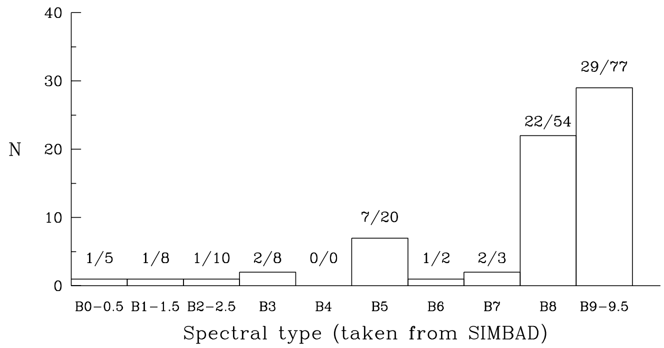

Figure 5. Histogram of the analyzed stars within the GAUDI B star sample. The ratio marked above each bin indicates the number of analyzed targets compared to the total amount that was available before the selection procedure, e.g., 1/5 means that there were 5 objects with this spectral type in the database, but that, for certain reasons, we were only able to analyze 1 of them. In total, 66 out of 187 objects could be analyzed.

The corresponding physical parameters are listed in Table 3, which summarizes the derived stellar parameters of the analysed GAUDI B type stars. All other spectral line fits, and their corresponding parameters, can be found at http://www.ster.kuleuven.be/~karolien/AnalyseBstar/Bstars/.

3.2.2. Comments on individual stars

In what follows, we discuss a few of the sample stars individually, because of certain particularities,

HD 45284. The derived effective temperature is in complete agreement with what was found by Hubrig et al. (2006). This star is an SPB exhibiting a magnetic field. The combination of the effective temperature and gravity resulting from Geneva photometry (Hubrig et al. 2006) positions the star just outside the main sequence towards the high-gravity side. Now, with our newly derived $\log g$, it falls within the expected instability domain of the SPB stars.

HD 46616 (B8) is a clear example of a He-weak star: all He I-lines have extremely low equivalent widths compared to 'normal' B stars. Even though the hydrogen and Si lines fit nicely, the He lines are predicted too strong in our grid models[5].

HD 48106 (B8) is oxygen poor based on the non-detection of the O I 7771-7775 triplet and is either He weak or Si strong. We were unable to fit both the He and Si lines at the same time.

For HD 46340 (B8), only He I 4471 and Si II 5041-5056 are visible. This was only sufficient to make a very rough estimate of the fundamental parameters: $T_{\rm eff} \approx 10\,000$ K, $\log g \approx 4.1$, negligible wind, solar He abundance.

[5] the lowermost considered He-abundance in our grid is n(He)/n(H)=0.1, see Section B.8.

On the hot side of the B-type domain, the analysis of the early type stars (e.g., HD 172488 (B0.5 V), HD 52918 (B1 V) and HD 173198 (B1 V)) show similar difficulties. The iterative procedure tends to yield too low temperatures due to the lower weight of the Si IV and He II lines as we have only one weak line. As only Si III is reliable and He I is not much affected by the effective temperature in this range, we are not able to derive trustworthy results.

HD 173370 (B9 V) shows a double peaked Hα profile. This morphology is typical for a very fast rotator (in this case, $v \sin i \approx 280$ km s^{-1}), seen almost equator-on. The disk-like feature also strongly affects the Hβ and Hγ profiles.

We also found a few chemically peculiar stars among the B stars in the GAUDI database. They are HD 44948 (B8 Vp), HD 45583 (B8), HD 46616 (B8) and HD 44907 (B9). They have a very rich spectrum, with a forest of sharp spectral lines, complicating the continuum determination and the fitting process, as almost all lines are blended. The He lines of HD 45583 are extremely weak and those of HD 46616 even completely vanished. Following Landstreet (2007), HD 45583 is a periodically variable Ap star. The line spectrum is completely distorted, hence too complicated to fit. The Si II lines are very strong, which indeed points towards a B8 or even B9 star.

4. Statistical properties of the sample and physical interpretation

4.1. Effective temperature scale

To derive a reliable calibration for the effective temperature as a function of the spectral subclass for B dwarfs, we need enough stars for which we have accurate information for both parameters. Unfortunately, this prerequisite is not fulfilled for our sample, as can be seen from the very large scatter around the existing spectral-type-$T_{\rm eff}$-calibrations, presented in Fig. 9. The scatter is due to uncertain effective temperatures for some targets and wrong spectral type designation for others. Indeed, for several stars, we encountered problems in the analysis, primarily because of the absence of Si lines for many fast-rotating late B type stars. These stars are too cool to have Si III present in their line spectrum, and the Si II lines are completely smoothed, so that they become hardly detectable. Even when they are still visible, the two lines of the Si II 4128-4130 doublet are so heavily blended that they cannot be used any longer. In these cases, the He I lines are the only lines that can be used to estimate the effective temperature, which are, therefore, not reliable enough to use in the derivation of an accurate temperature calibration. On the other hand, several stars for which we were able to derive accurate values for the effective temperature turned out to have completely wrong spectral types. We caution the use of spectral types as they are quite often derived from low-resolution and low-quality spectra. Flags and remarks on the fit quality of individual targets were added in Table 3.

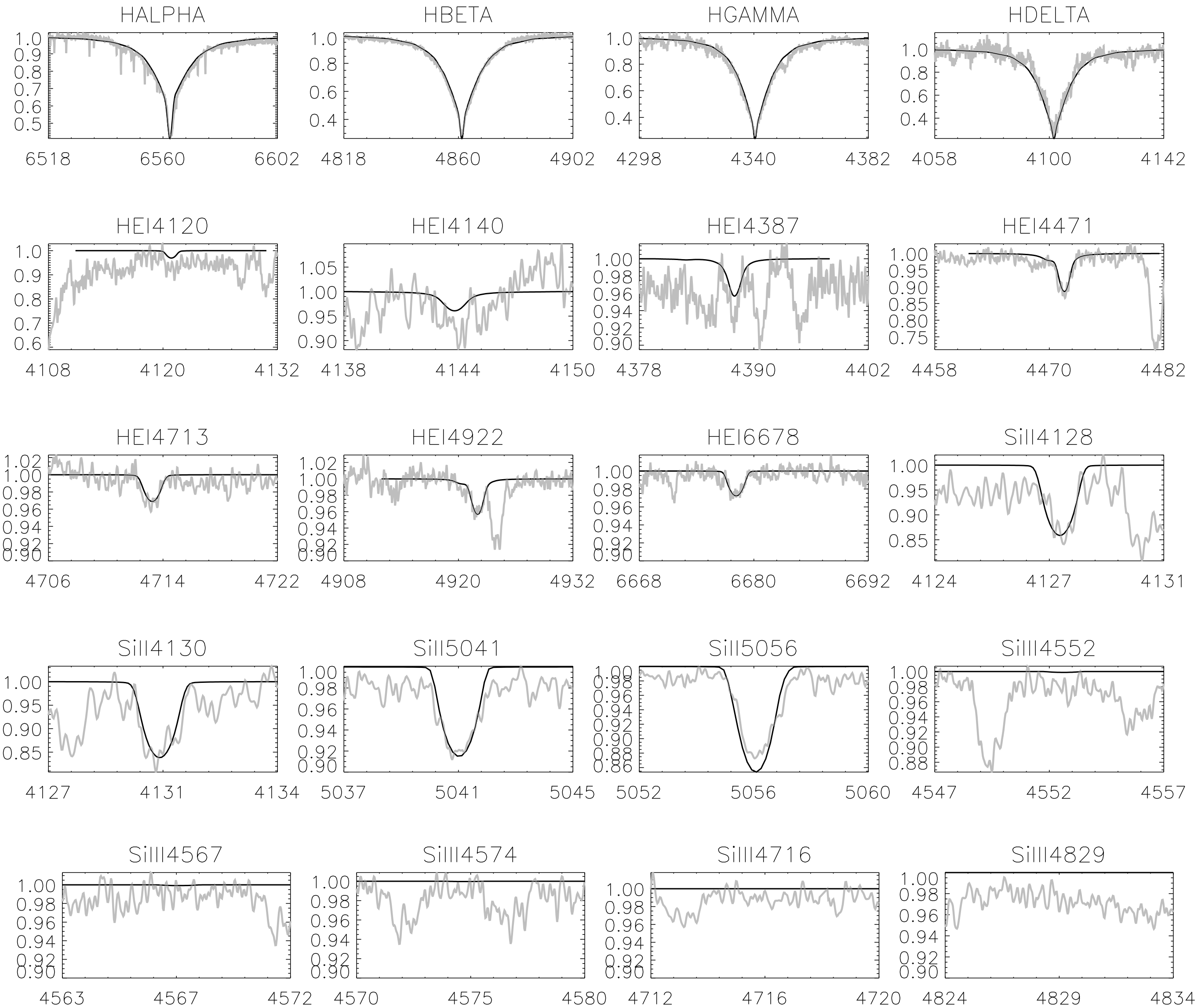

Figure 6. Example of the line profile fits for *a 'cool' giant* which has, meanwhile, been observed by CoRoT (Miglio et al., in preparation): HD 181440 (B9 III). Despite the low quality of the data, and the fact that we have no more Si III left in this temperature region, we are still able to obtain a satisfying solution.

4.2. The stars in the ($T_{\rm eff}$, $\log g_c$)-diagram

Fig. 10 shows the ($T_{\rm eff}$, $\log g_c$)-diagram of the analyzed GAUDI stars, along with the position of instability strips. The latter were computed with the evolutionary code CLÉS (Scuflaire et al. 2008) and the pulsation code MAD (Dupret et al. 2002), respectively. These strips were computed for a core-overshoot parameter of 0.2 times the local pressure scale height (Miglio et al. 2007a,b). It was indeed found from seismic modeling of B type stars that core overshooting occurs, on average with such a value (Aerts 2008). We thus compare the position of the GAUDI stars with the most recent models tuned by asteroseismology.

For 40% of the GAUDI stars (26 out of 66), we have information on the luminosity class. All but one (i.e. 9 out of 10) with known luminosity class II or III are indeed situated beyond the Terminal Age Main Sequence (TAMS hereafter), so we confirm them to be giants. The only exception is HD 49643, a star of spectral type B8 IIIn, i.e. with spectroscopic lines which may originate from nebulosity. The star is a fast rotator with a $v \sin i$ of almost 300 km s^{-1}. The absence of Si lines due to the high rotation implies less reliable estimates for $T_{\rm eff}$ and $\log g$ than for the bulk of the sample stars. Thus, its derived gravity of 3.70 dex might be compatible with its previous classification as a giant.

Three of the 14 stars with luminosity class IV or V turn out to be giants, i.e. they have – within the error bars – a surface gravity $\log g_c$ below 3.5. It concerns HD 43461 (B6V), HD 50251 (B8V), and HD 182198 (B9V), of which HD 43461 is a fast rotator and has, therefore, less reliable parameters due to the absence of Si lines. Regarding the other two stars, there is a certain possibility that they are fast rotators as well, observed almost pole-on. Due to centrifugal effects, the stellar surface would become distorted, and effective tempera-

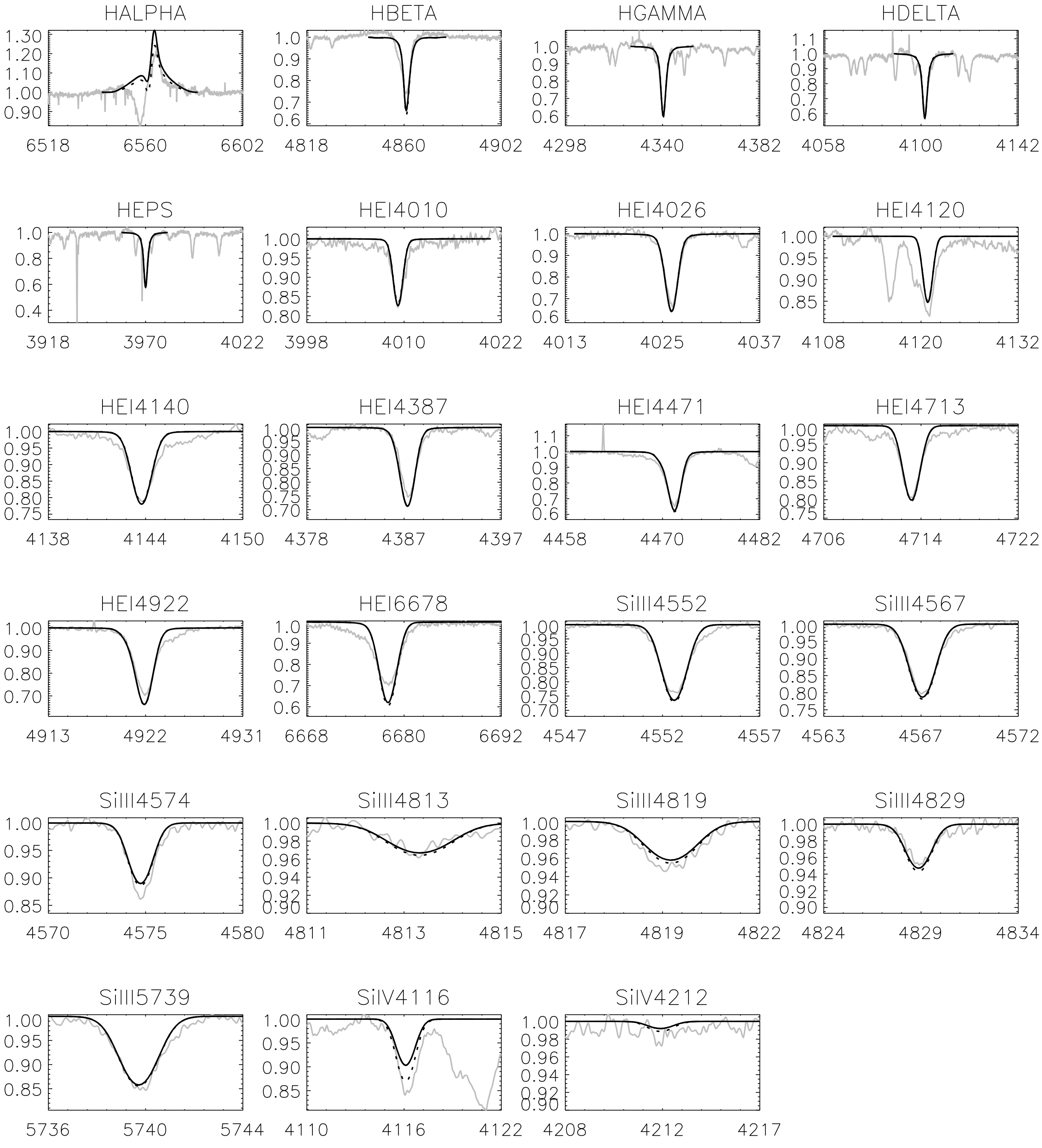

Figure 7. Example of the line profile fits for the only *hot supergiant* in our sample: HD 52382 (B1Ib). While the peak of Hα is reasonably well reproduced, the blue-ward absorption trough cannot be fitted at the available grid combinations of wind strength parameter and wind velocity field exponent. Note that no interpolation is performed for these quantities, and that the wind is considered as unclumped, which might explain the obvious mismatch (e.g., Puls et al. 2006, in particular their Fig. 7). The Balmer lines show bumps in the wings. It is not clear whether this is real and due to the strong wind, or if this is a spectral artefact. It also arises in the only cool supergiant in our sample. The interpolated Si abundance (log n(Si)/n(H) = −4.67) is higher than the closest grid abundance (log n(Si)/n(H) = −4.79, plotted here), which explains the observed discrepancies in the Si line cores. In dotted lines, we show the line profiles as they would appear with the interpolated parameters.

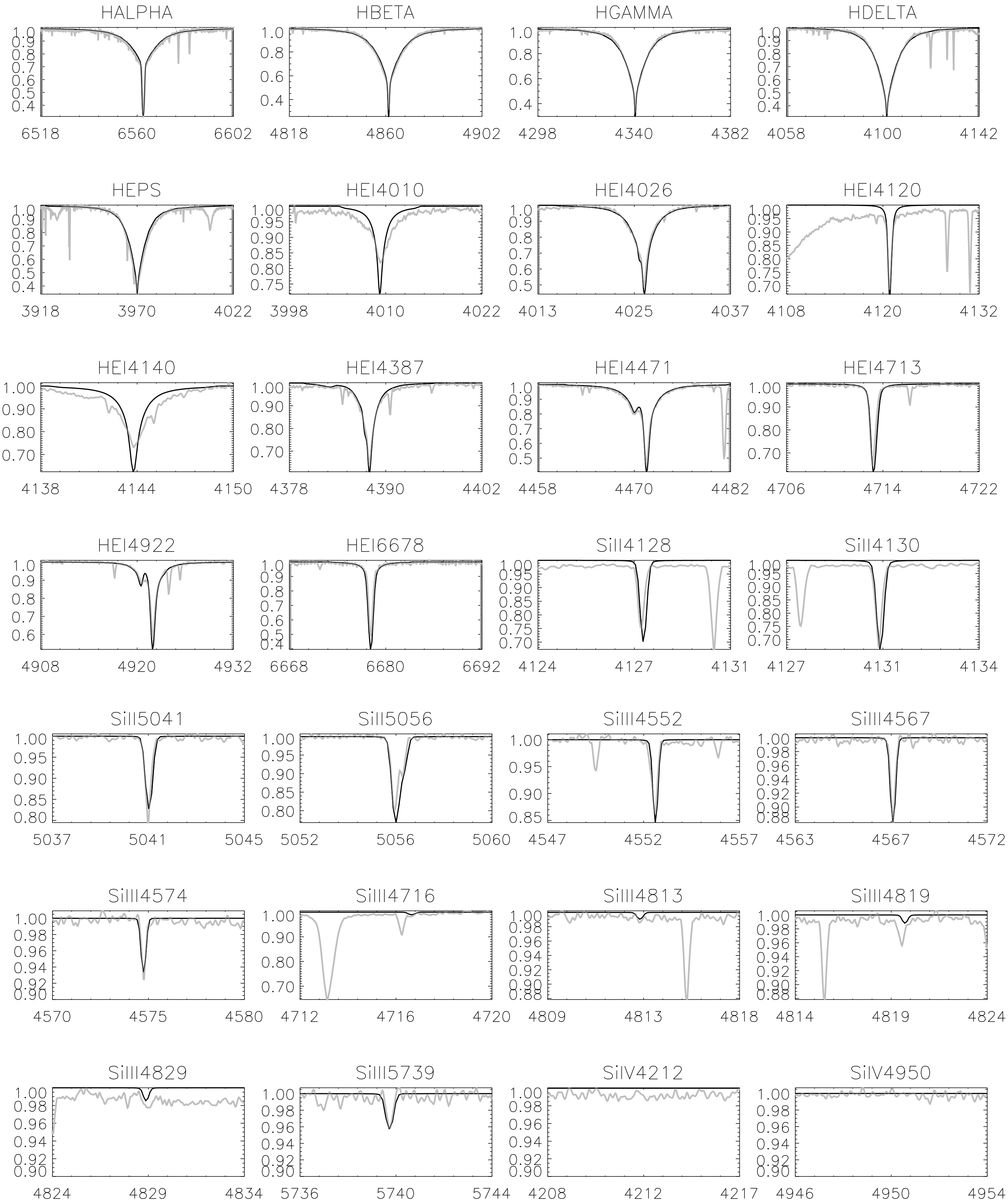

Figure 8. Example of the line profile fits for an *intermediate hot dwarf*: HD 44700 (B3 V). The strong lines on the blue side of Si III 4716 and Si III 4819 are easily mistaken for the Si lines themselves. This is the reason why we always indicate the exact position of the transition during the full preparation process. The misfit of He I 4010 and 4140 is due to incomplete broadening functions of these lines. These lines were not used during the fitting procedure, but only as a double check afterwards (see Appendix B.1). We observe a similar behavior in several other stars. All other lines, even the weakest, fit very well. The shape of He I 4471 is even perfect.

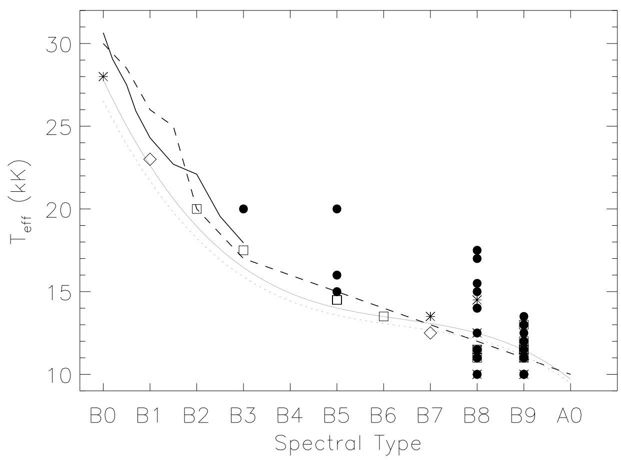

Figure 9. Effective temperature as a function of spectral type. We compare the position of our sample stars to existing temperature scales: for Galactic dwarfs, for spectral types up to B3 (Trundle et al. 2007, solid black line), for dwarfs in the entire B type domain (Crowther 1998, dashed black line), for Galactic B supergiants (Lefever et al. 2007b, dotted grey line) and for Galactic and SMC B supergiants (Markova & Puls 2008, solid grey line). Due to wind blanketing effects, the calibrations for the B supergiants lie at lower temperatures than the calibrations for B dwarfs. The supergiants (l.c. I) are indicated by diamonds, the (sub)giants (l.c. II and III) by asterisks and the (sub)dwarfs (l.c. IV and V) by squares. Filled circles indicate the stars for which we do not have any a priori information on luminosity class. It can be seen that spectral types taken from the literature can be quite inaccurate (see text).

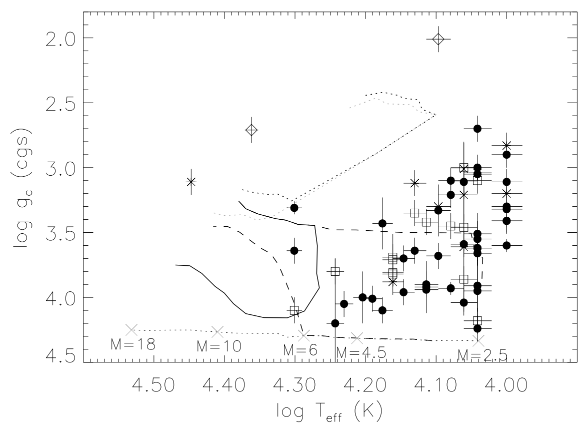

Figure 10. ($T_{\rm eff}$, $\log g_c$) diagram of the analyzed GAUDI B stars, with the corresponding 2σ-error bars. Symbols are the same as in Fig. 9. The dotted line represents the ZAMS, and five initial ZAMS masses - in $M_\odot$ - have been indicated. The most recent theoretical instability domains for the β Cephei (thick solid line) and the SPB stars (dashed lines) for main-sequence models, with a core overshooting value of 0.2 times the local pressure scale height, are shown (Miglio et al. 2007a,b), together with the instability domains for post-TAMS models with $\ell = 1$ (grey dotted) and $\ell = 2$ (black dotted) g-modes computed by Saio et al. (2006). The TAMS is shown as the low-gravity edges of the SPB and β Cephei instability domains around $\log g_c = 3.5$.

ture (due to gravity darkening) and surface gravity increase towards the pole. If observed pole-on, both quantities might be underestimated with respect to their average values. On the other hand, also the main sequence gets extended compared to standard models when rotation is taken into account (e.g., Maeder & Meynet 2000). Similar results to ours were obtained by Hempel & Holweger (2003), who found 6 out of their 27 sample stars with spectral type from B6V to B9V to have a $\log g$ below 3.5.

Depending on the input physics, stellar evolution theory shows that roughly 10 – 20% of the B8-B9 stars are in the giant phase, but only 2 to 5% of B0-B3 stars (e.g., Prialnik 2000; Scuflaire et al. 2008). >From the 40 stars without luminosity class treated by us, 11 turn out to be beyond the main sequence. From the 14 dwarfs, 3 turn out to be giants as well, and from the 10 giants, one turned out to be a dwarf instead. Thus our sample contains 23 giants, 19 of which have spectral type B8-B9. As our sample contains in total 51 stars of spectral type B8-B9, this means that the percentage of late type giants in our sample (37%) is about twice the expected one. Only five stars in our sample have spectral types earlier than B3, one of which is a giant, which is too low number statistics to verify the expected percentage. We found 20 of the 40 stars without luminosity class to have $v \sin i$ above 90 km s^{-1}, and for 8 of them even $v \sin i > 150$ km s^{-1}. This fast rotation may again explain why we observe twice the number of expected giants when comparing with standard models. Rotation was also found to be a necessary ingredient in evolutionary models in order to explain the number of observed giants in the well-studied open clusters h and χPer (Vrancken et al. 2000, in particular their Fig. 3).

4.3. The macroturbulent and rotational velocities

When comparing the rotational broadening with macroturbulence, we observe a systematic trend of increasing $v_{\rm macro}$ with increasing $v \sin i$ for those stars for which some pulsational behavior may be expected, i.e., for the stars where $v_{\rm macro}$ cannot be neglected (filled circles in Fig. 11). This is consistent with Markova & Puls (2008, and references therein), who found that, in almost all cases, the size of the macroturbulent velocity was similar to the size of the rotational velocity. On the other hand, they also found $v \sin i$ and $v_{\rm macro}$ to decrease towards later subtypes, being about a factor of two lower at B9 than at B0.5, and that, in none of their sample stars, rotation alone was able to reproduce the observed line profiles. We cannot confirm either of both statements, as we have found, on the contrary, many cases with zero macroturbulence, and many late B type stars with very high macroturbulent velocities. The trend connecting $v \sin i$ and $v_{\rm macro}$ suggests that both broadening mechanisms *are* difficult to disentangle. All '$v_{\rm macro}$'-values seem to be at least one third of $v \sin i$, as can be derived from the position of the filled circles above the dashed line in Fig. 11. From a certain projected rotational velocity on (i.e., around $v \sin i$

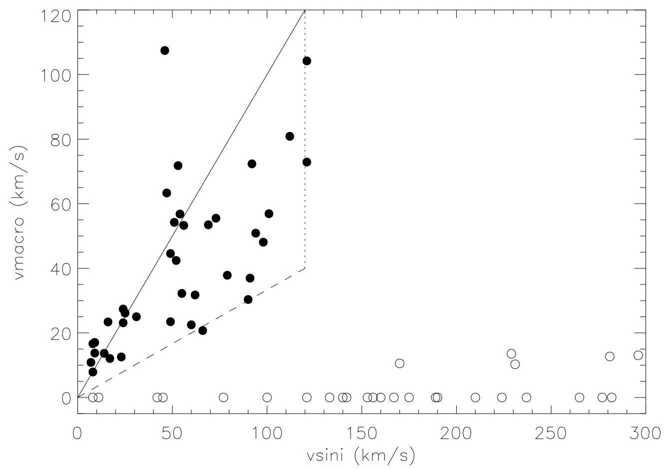

Figure 11. Comparison between the macroturbulence and the projected rotational velocity $v \sin i$. The solid line is the 1-1 relation, while the dashed line represents the relation $v_{\rm macro}/v \sin i = 1/3$. Those stars which we consider as non-pulsating (i.e., which have a negligible $v_{\rm macro}$) are indicated by open circles. The filled circles represent suspected pulsators (i.e., they have a significant $v_{\rm macro}$).

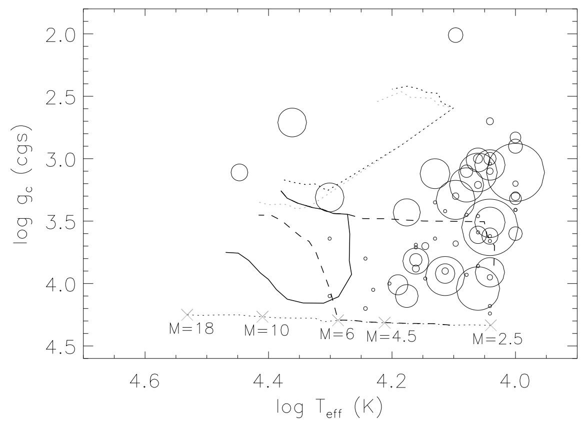

Figure 12. Same as Fig. 10, but representing the values of $v_{\rm macro}$ for the GAUDI B star sample. The size of the symbols is proportional to the $v_{\rm macro}$-value.

= 120 km s^{-1}, dotted vertical line), it is impossible to separate both effects, as the pulsational behavior (represented by $v_{\rm macro}$) completely disappears in the projected rotational broadening. Following the earlier argumentation that stars which have a non-negligible macroturbulent velocity may have the largest pulsational amplitudes, we investigated the behavior of $v_{\rm macro}$ in the ($T_{\rm eff}$, $\log g$)-plane (see Fig. 12). On a global scale, the $v_{\rm macro}$-values show a random spread. The position of some individual cases is intriguing, e.g., the supergiant HD 52382 (log $T_{\rm eff} \approx 4.36$, $\log g \approx 2.71$). The star's position is compatible with the occurrence of gravity modes excited by the opacity mechanism in evolved stars and may belong to a recently found class of pulsating B-type supergiants (Lefever et al. 2007b). As pointed out by Aerts et al. (2009), these gravity-mode oscillations may result in pulsational line broadening, hence the high $v_{\rm macro}$-value we find. HD 48807 (B7 Iab) and HD 48434 (B0 III) also show macroturbulence and may belong to the same class. Some of the dwarfs in the sample show macroturbulence, e.g., HD 48215 (B5 V), HD 177880 (B5 V) and HD 50251 (B8 V) might be g-mode pulsators in the SPB instability domain. Many stars with $\log g$ below 3.5 show a reasonable to large $v_{\rm macro}$, which may imply them to be pulsators. It is noteworthy that all instability computations for mid to late B stars so far have been computed for non-rotating models and were stopped artificially at the TAMS from the argument that no star is expected to be found in the Hertzsprung gap. B8 to B9 stars, however, cross this gap at a much lower pace than stars with spectral type earlier than B7 and our observational spectroscopic results point out that it would be worthwhile to extend the instability strip computations past the TAMS.

Finally, the magnitude of the microturbulence seems to be randomly distributed in the ($T_{\rm eff}$, $\log g$)-diagram, and in no way related to the effective temperature nor the surface gravity (see Fig. 13).

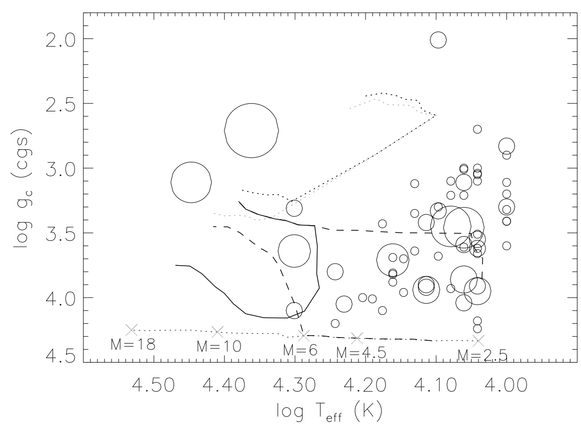

Figure 13. Same as Fig. 12, but the size of the symbols is now proportional to the microturbulent velocity ξ of the GAUDI B star sample.

5. Future use of our results

The GAUDI database was set up during the preparation of the CoRoT space mission. We applied our developed automated tool for the determination of the fundamental parameters to numerous B stars in this database. A recent independent study used the same database to determine the abundances of the 89 B6-B9 stars in GAUDI, using a different approach based on LTE atmosphere models without wind and LTE occupation numbers. We refer to Niemczura et al. (2009) for the underlying assumptions, but mention here that a mild depletion of both Fe and Si, with average values of the iron and silicon abundances of 7.13±0.29 dex and 7.22±0.31 dex, respectively, was found for their sample. This result was obtained from spectrum synthesis in the LTE approximation, by fixing the effective temperatures from photometric calibrations, the microturbulence at 2 km s^{-1} and ignoring any macroturbulence in the line profile fits. The mild Si depletion is in agreement with our results for the Si abundance of the late B stars treated by us.

Meanwhile the first data of CoRoT were released to the public. Two of our sample stars were already observed by the satellite. It concerns HD 181440 (B9 III) and HD 182198 (B9 V). The spectra of these stars were available in the GAUDI database and their parameters are listed in Table 3. Their seismic analysis is under way (Miglio et al., in preparation).

We also point out that one of the primary targets of CoRoT is HD 180642 (B1.5 II-III), which is a mildly N-enriched, apparently slowly rotating β Cephei star, discovered by Aerts (2000). Morel & Aerts (2007) determined its fundamental parameters from high-resolution spectroscopy and derived $T_{\rm eff}$ = 24 500 ± 1 000 K and logg = 3.45 ± 0.15, ξ = 12 ± 3 km s^{-1}. By means of AnalyseBstar, we found the model with $T_{\rm eff}$ = 24 000 ± 1 000 K, logg = 3.40 ± 0.10 and ξ = 13 ± 2 km s^{-1} to be the best fitting one, so our results agree very well with theirs. We thus classify this star as a pulsator very close to the TAMS. It will be very interesting to know if this spectroscopic result will be confirmed by the seismic modeling of oscillation frequencies derived from the CoRoT space photometry, because this would imply one of the few β Cephei stars very close to the end of the core-hydrogen burning stage.

At the time of launch, the CoRoT space mission was nominally approved to operate through 2009, but, given its excellent performance, the operations will probably be prolonged. It is therefore to be expected that several more B-type stars in GAUDI will be observed by the mission in the near future.

Acknowledgements. The research leading to these results has received funding from the European Research Council under the European Community's Seventh Framework Programme (FP7/2007–2013)/ERC grant agreement n°227224 (PROSPERITY), as well as from the Research Council of K.U. Leuven grant agreement GOA/2008/04. The authors wish to thank Alex de Koter cordially for insightful discussions and helpful comments throughout the project. The authors would like to thank the anonymous referee for valuable comments and suggestions on how to improve this paper.

References

Aerts, C. 2000, A&A, 361, 245

Aerts, C. 2008, in IAU Symposium, Vol. 250, IAU Symposium, 237–244

Aerts, C. & De Cat, P. 2003, Space Science Reviews, 105, 453

Aerts, C., Puls, J., Godart, M., & Dupret, M. 2009, A&A, in press [astroph/0909.3585]

Briquet, M. & Morel, T. 2007, Communications in Asteroseismology, 150, 183

Butler, K. & Giddings, J. R. 1985, in Newsletter on Analysis of Astronomical Spectra, No. 9, Univ. London

Crowther, P. A. 1998, in IAU Symposium, Vol. 189, Fundamental Stellar Properties, ed. T. R. Bedding, A. J. Booth, & J. Davis, 137

Decin, L., Hony, S., de Koter, A., et al. 2007, A&A, 475, 233

Desmet, M., Briquet, M., Thoul, A., et al. 2009, MNRAS, 396, 1460

Dufton, P. L., Smartt, S. J., Lee, J. K., et al. 2006, A&A, 457, 265

Dupret, M., De Ridder, J., Neuforge, C., Aerts, C., & Scuflaire, R. 2002, A&A, 385, 563

Evans, C. J., Smartt, S. J., Lee, J.-K., et al. 2005, A&A, 437, 467

Frémat, Y., Neiner, C., Hubert, A.-M., et al. 2006, A&A, 451, 1053

Fridlund, M., Baglin, A., Lochard, J., & Conroy, L., e., eds. 2006, ESA Special Publication, Vol. 1306, The CoRoT Mission - Pre-Launch Status - Stellar Seismology and Planet Finding

Giddings, J. 1981, PhD thesis, University of London, UK

Gräfener, G., Koesterke, L., & Hamann, W.-R. 2002, A&A, 387, 244

Gray, D. F. 1973, ApJ, 184, 461

—. 1975, ApJ, 202, 148

—. 1976, The observation and analysis of stellar photospheres (New York, Wiley-Interscience)

Handler, G., Jerzykiewicz, M., Rodríguez, E., et al. 2006, MNRAS, 365, 327

Hauschildt, P. & Baron, E. 1999, J. Comp. Appl. Math., 109, 41

Hempel, M. & Holweger, H. 2003, A&A, 408, 1065

Hillier, D. J. & Miller, D. L. 1998, ApJ, 496, 407

Hubeny, I. & Lanz, T. 2000, Bulletin of the American Astronomical Society, 32, 1531

Hubrig, S., Briquet, M., Morel, T., et al. 2008, A&A, 488, 287

Hubrig, S., Briquet, M., Schöller, M., et al. 2006, MNRAS, 369, L61

Hunter, I., Brott, I., Lennon, D. J., et al. 2008a, ApJ, 676, L29

Hunter, I., Dufton, P. L., Smartt, S. J., et al. 2007, A&A, 466, 277

Hunter, I., Lennon, D. J., Dufton, P. L., et al. 2008b, A&A, 479, 541

Kudritzki, R. & Puls, J. 2000, ARA&A, 38, 613

Kurucz, R. L. 1993, CD-ROM 13 (Cambridge: SAO)

Lefever, K. 2007, PhD thesis, Institute of Astronomy, K.U.Leuven, Belgium

Lefever, K., Puls, J., & Aerts, C. 2007a, in Astronomical Society of the Pacific Conference Series, Vol. 364, The Future of Photometric, Spectrophotometric and Polarimetric Standardization, ed. C. Sterken, 545

Lefever, K., Puls, J., & Aerts, C. 2007b, A&A, 463, 1093

Levenberg, K. 1944, The Quarterly of Applied Mathematics, 2, 164

Maeder, A. & Meynet, G. 2000, ARA&A, 38, 143

Markova, N. & Puls, J. 2008, A&A, 478, 823

Marquardt, D. 1963, SIAM J. Appl. Math., Volume 11, Issue 2, 431

Massey, P., Zangari, A. M., Morrell, N. I., et al. 2009, ApJ, 692, 618

Mazumdar, A., Briquet, M., Desmet, M., & Aerts, C. 2006, A&A, 459, 589

Miglio, A., Montalbán, J., & Dupret, M.-A. 2007a, MNRAS, 375, L21

—. 2007b, Communications in Asteroseismology, 151, 48

Mokiem, M. R., de Koter, A., Puls, J., et al. 2005, A&A, 441, 711

Morel, T. & Aerts, C. 2007, Communications in Asteroseismology, 150, 201

Morel, T., Butler, K., Aerts, C., Neiner, C., & Briquet, M. 2006, A&A, 457, 651
—. 2007, Communications in Asteroseismology, 150, 199
Morel, T., Hubrig, S., & Briquet, M. 2008, A&A, 481, 453
Neiner, C., Hubert, A.-M., & Catala, C. 2005, ApJS, 156, 237
Niemczura, E., Morel, T., & Aerts, C. 2009, A&A, 506, in press [astroph/0909.4934]
Pauldrach, A. W. A., Hoffmann, T. L., & Lennon, M. 2001, A&A, 375, 161
Prialnik, D. 2000, An Introduction to the Theory of Stellar Structure and Evolution (Cambridge, UK: Cambridge University Press)
Przybilla, N., Nieva, M.-F., & Butler, K. 2008, ApJ, 688, L103
Puls, J., Markova, N., Scuderi, S., et al. 2006, A&A, 454, 625
Puls, J., Urbaneja, M. A., Venero, R., et al. 2005, A&A, 435, 669
Repolust, T., Puls, J., Hanson, M. M., Kudritzki, R.-P., & Mokiem, M. R. 2005, A&A, 440, 261
Saio, H., Kuschnig, R., Gautschy, A., et al. 2006, ApJ, 650, 1111
Santolaya-Rey, A. E., Puls, J., & Herrero, A. 1997, A&A, 323, 488
Scuflaire, R., Théado, S., Montalbán, J., et al. 2008, Ap&SS, 316, 83
Simón-Díaz, S. & Herrero, A. 2007, A&A, 468, 1063
Solano, E., Catala, C., Garrido, R., et al. 2005, AJ, 129, 547
Trundle, C., Dufton, P. L., Hunter, I., et al. 2007, A&A, 471, 625
Urbaneja, M. A. 2004, PhD thesis, Instituto de Astrofisica de Canarias, Spain
Vrancken, M., Lennon, D. J., Dufton, P. L., & Lambert, D. L. 2000, A&A, 358, 639

Online Material

Appendix A: Formal convergence tests for synthetic FASTWIND spectra – some details

Before applying AnalyseBstar to real, observed spectra, we first tested whether the method is able to recover the input parameters of synthetic spectra. For this purpose, we have created several synthetic datasets in various regions of parameter space. We will not dwell on discussing all of them here, but we have chosen three specific examples, each representative for a different type of star:
- Dataset A: a B0.5 I star with a rather dense stellar wind and a strongly enhanced helium abundance,
- Dataset B: a B3 III star with a weak stellar wind and a depleted Si abundance
- Dataset C: a B8 V with a very thin stellar wind.

Each dataset has been convolved with both a rotational and a macroturbulent broadening profile. The projected rotational velocity adopted is 50 $\mathrm{km\,s^{-1}}$ for each dataset, characteristic for a 'typical' slow rotator. In the case of low and intermediate resolution spectra, there is also the possibility to carry out an additional Gaussian, instrumental convolution. This is, however, not necessary for spectra with such high resolution as FEROS and ELODIE. Artificial (normally distributed) noise was added to mimic a real spectrum with a mean local SNR of 150, which is more or less the minimal local SNR obtained for the GAUDI sample.

Finally, we have gone through the full process of the preparation of the spectra as if it were real data, i.e., defining the EW of all available lines, measuring the SNR to account for the errors on the EW and fixing the projected rotational velocity. Since we are dealing with synthetic data, obviously no normalization was required.
Table A.1 lists the input parameters for the three synthetic datasets as well as the output parameters, obtained from the application of AnalyseBstar. For each dataset, the second column gives the derived 'interpolated' values, while the third column lists the parameters of the closest (best fitting) grid model. In the ideal case, both should be exactly the same as the input parameters. This depends, however, on how well the equivalent widths were measured and minor deviations occur as expected. Besides these three cases, in which we started from a synthetic model which is one of the grid points, we have additionally created three synthetic datasets for which the parameters lie in between different grid points. In analogy to datasets A to C, their profiles have been convolved with both a rotational and macroturbulent broadening profile and artificial noise was added. The input parameters and the results of the analysis have been added to Table A.1 as datasets D, E and F.
A third set of models (G, H, I) consists of models computed for parameters not included in the grid, but within the grid limits, and this time without noise, with the aim to test the predictive power of our method, independent of the source of errors introduced by the noise. The rotational velocity applied for these test models is 30 $\mathrm{km\,s^{-1}}$, and the macroturbulent velocity is 15 $\mathrm{km\,s^{-1}}$. We find an overall very good agreement of the closest grid model and the interpolated values with the input parameters.

Although the models given in Table A.1 were selected as the best fitting models, the program additionally came up with some other models, which agree with the input model within the errors, introduced by the artificial noise and the errors in the determination of the equivalent widths (datasets A to F) and/or the various interpolations (datasets D to I). For instance, for dataset I, AnalyseBstar came up with a second possibility with slightly different parameters, even closer to the input data: $\log g$ = 1.7, ξ = 6.5 $\mathrm{km\,s^{-1}}$, v_{macro} = 14.6 $\mathrm{km\,s^{-1}}$, $N(He)/N(H)$ = 0.12, but with log n(Si)/n(H) = -4.49 (the other parameters are the same as the ones for the model in the table). As the Si abundance is overestimated compared to the input value, the Si lines are overall a bit too strong and the final fit is slightly worse than the one for the model in the table.

In all nine cases, the input parameters are well recovered. Typically 10 to 150 models are selected and considered during the analysis cycle. The number depends not only on the choice of the initial parameters, but also on the accuracy of the measured quantities and the applied procedure (hence, the temperature domain, see below). We considered numerous other test cases, which are not included in this text, but for which the input parameters were equally well recovered. Slight deviations from the input parameters are as expected. Also in the cool temperature domain (datasets C, F and I), where our alternative optimization 'method 2' is required (see Section B.3), we are still able to deduce reliable parameter estimates, at least for the synthetic models. The results for the Si abundance in datasets F clearly show the problem for estimating the abundances when only one ion is present: the estimation of the Si abundance was, for this particular test case, not equal to the input value. When we have only Si II lines, the results cannot be as secure as when we have two ionisation stages of Si. This problem has been accounted for by adopting somewhat larger errors on the derived parameters, for objects with $T_{\mathrm{eff}} < 15\,000$ K (see Table 3).
When the observed object is close to one of the borders of the grid, the method takes 'the border' as the closest match. This will, consequently, lead to larger errors in some of the other parameters.

The derived $v \sin i$ -value, which is difficult to disentangle from the macroturbulent velocity, agrees very well with the inserted values, irrespective of v_{macro}. This shows that the Fourier Transform method indeed allows to separate both effects. All together, this gives us confidence that our method is working reliably and that the procedure will also be able to recover the true physical parameters from real spectra.

The macroturbulent velocity is the only fit parameter for which significant deviations arise, if v_{macro} is low (< 30 $\mathrm{km\,s^{-1}}$). Larger macroturbulences are well recovered, however. Especially for datasets C, E and I, where v_{macro} is only 10-15 $\mathrm{km\,s^{-1}}$, the deviation is large (of the order of 15 to 30 $\mathrm{km\,s^{-1}}$). To understand this discrepancy, we first had a look at the line profiles, which show that the fit is almost perfect for this v_{macro} (see Fig A.1). After verifying the fit quality, we also verified that the discrepancies do not arise from our applied procedure, by performing several tests on simulated spectra, in which we left v_{macro} as the only free parameter. In all cases, the macroturbulent velocity was recovered very well, with deviations within 5 $\mathrm{km\,s^{-1}}$. The (sometimes significant) deviations in

$v_{\rm macro}$ can be understood as a compensation for differences between the interpolated values of the 'observed' line profiles and the closest grid model. Indeed, as shown by Aerts et al. (2009), small deviations in the wings of the Si profiles can result in wrong estimates of $v_{\rm macro}$ and $v \sin i$, because these two velocity fields are hard to disentangle whenever one of them is small. Thus, the values derived for $v_{\rm macro}$ should be treated with caution. This does not affect the derivation of the other parameters, however, since a convolution with the $v_{\rm macro}$-profile preserves the EW of the lines. It is the EW, and not the line profile shape, which is used for the derivation of $T_{\rm eff}$, ξ and log n(Si)/n(H). The other parameters (gravity, mass-loss rate, and wind velocity law) remain unaffected because they are deduced from the Balmer lines, which are not very sensitive to the $v_{\rm macro}$ values due to the dominance of the Stark broadening. Thus we find a very good agreement between their input and output values (Table A.1).

Appendix B: Methodology of AnalyseBstar

In what follows, we give a detailed description of AnalyseBstar. In Fig. B.1, a flowchart of the full program is drawn schematically. The reader is advised to follow this context diagram throughout the further description of AnalyseBstar.

B.1. Preparation of the input

No automatic method can fully replace the 'by-eye' procedure, and this is also true for AnalyseBstar. A few steps still require human intervention. This especially concerns the preparation of the spectra and the input for the main program, as will be shown in the following.

Observation of peculiarities. The first thing to be done when starting the analysis is to inspect the spectrum regarding any 'abnormalities', such as line behavior resulting from nebulae, disks, binarity or other peculiarities. Special features can and should be detected through eye inspection.

Merging and normalization of the spectra. When dealing with échelle spectra, like the ELODIE and FEROS spectra in the GAUDI database, we first need to merge the spectral orders before the spectrum can be normalized. This is a very delicate and non-trivial process. The edges of the orders are often noisy, due to the decrease in sensitivity of the CCD near its edges, and are therefore removed. Spectral lines falling inconveniently on the edge of one spectral order or in the overlap region of two consecutive orders, thus resulting in a cut-off within the spectral line, are not reliable to derive accurate stellar information. They can, in the best case, only be used for a consistency check afterwards. After the spectra have been merged, they are normalized through interactive interpolation of continuum regions. This is done over a large wavelength coverage, where sufficient continuum regions are present, in order to avoid line corruption which will propagate in the derivation of the fundamental parameters. The normalization especially proves to be very important for the determination of the gravity, which depends sensitively on the Balmer line wings.

Radial velocity correction. The spectra need to be corrected for radial velocity shifts. Shifting the spectrum to rest wavelength automatically has not been included in the current version yet.

Line selection. As a standard procedure, we compute a number of line profiles in the optical from the underlying model atmosphere. These standard line profiles can be used directly. Computing additional line profiles is, however, straightforward. The selection of lines to be used during the spectral analysis in AnalyseBstar is gathered from a file which contains a default (but easily editable) list of currently used optical lines (see below). We distinguish between optical lines that will be used for the prediction of the physical parameters during the spectral line fitting procedure and those that will not be used explicitly for reasons of uncertainties, either in the theoretical predictions or in the observed spectrum (due to problems in merging or normalization). The goodness-of-fit of the latter lines is only checked to investigate systematic differences between theory and observations, which can be useful input for considerations regarding further improvements of atomic data and/or atmospheric models. They are Hϵ, He I 4010, 4120, 4140 and Si IV 4950. The lines that *will* be used in the fitting procedure for their predictive power are the following: the Balmer lines Hα, Hβ, Hγ and Hδ, the neutral and singly ionized He lines He I 4026, 4387, 4471, 4713, 4922, 6678, He II 4541 and He II 4686, and the Si lines in their three different ionization stages Si II 4128-4130, Si II 5041-5056, Si III 4552-4567-4574, 4716, 4813-4819-4829, 5739, Si IV 4116 and Si IV 4212. He II 4200 was excluded as it can only safely be used for O-type stars and not for B-type stars. At least for dwarfs, it only appears at temperatures above about 25 000 K, where it is still overruled by N II, while at hotter temperatures, He II 4200 is for 50% blended by N III[6].

Signal-to-noise measurement. To estimate the error on the equivalent width as accurate as possible, we need to determine the signal-to-noise ratio, SNR. Since the SNR can vary a lot with wavelength, we chose to calculate the *local* SNR for each line separately, by using a continuum region close to the line. This is done manually through the indication of the left and right edges of the continuum interval. The SNR is then given by the mean flux $\overline{F_c}$ divided by the standard deviation $\sigma(F_c)$ of the flux in this interval, i.e.,

$$\mathrm{SNR} = \overline{F_c}/\sigma(F_c).$$

Observed equivalent widths and their errors (cf. Fig. B.2). The equivalent widths of most He and Si lines can be measured by a Gaussian non-linear least squares fit to the observed line profiles, using the Levenberg-Marquardt algorithm (Levenberg 1944; Marquardt 1963). We thoroughly tested whether this was

[6] See http://www.lsw.uni-heidelberg.de/cgi-bin/websynspec.cgi

Table A.1. Input parameters for the synthetic models (IN) are compared to the actual output parameters (OUT) obtained through the application of AnalyseBstar to these synthetic data: the effective temperature, $T_{\rm eff}$, the surface gravity, $\log g$, the wind strength parameters, log Q (see below), the wind velocity exponent, β, the He abundance, n(He)/n(H), the Si abundance, log n(Si)/n(H), the microturbulent velocity, ξ, the projected rotational velocity, $v \sin i$, the macroturbulent velocity, $v_{\rm macro}$, the time elapsed in seconds during the run of AnalyseBstar, and the number of different models that have been checked throughout the procedure. The wind strength parameter log Q is given by $\log \dot{\rm M}/(v_\infty\,{\rm R}_*)^{1.5}$, where $\dot{M}$ is the mass-loss rate, v_∞ the terminal wind velocity, and R_* the stellar radius. In our grid, we allow for 7 different values, represented by a character: log Q = -14.30 (O), -14.00 (a), -13.80 (A), -13.60 (b), -13.40 (B), -13.15 (C), -12.70 (D).
Datasets A, B, and C are models which lie exactly on a grid point, whereas dataset D, E, and F are models which lie in between the gridpoints. Artificial noise was added to the synthetic line profiles in these two datasets, to simulate a real spectrum. The models for datasets G, H, and I also lie in between the gridpoints, but no artificial noise was added and a lower $v \sin i$ (30 km s^{-1} instead of 50 km s^{-1}) was used in order to test the predictive capabilities of the method. The 'interpolated' values derived for the parameters, as well as the best fitting (i.e. closest) grid model are given. The parameters in italics are those for which no real interpolation was made, but for which the most representative grid value is chosen. The longer computation times for the cooler models are due to the different method applied in this range.

	IN	OUT inter-polated	OUT grid	IN	OUT inter-polated	OUT grid	IN	OUT inter-polated	OUT grid
fit parameter	Dataset A			Dataset B			Dataset C		
$T_{\rm eff}$ (K)	23,000	22,600	23,000	18,000	18,100	18,000	13,000	*13,000*	13,000
$\log g$ (cgs)	2.7	*2.7*	2.7	3.3	*3.3*	3.3	4.2	*4.2*	4.2
$\log Q$ (char)	C	*C*	C	A	*b*	b	O	*a*	a
β	2.0	*2.0*	2.0	1.5	*1.2*	1.2	0.9	*0.9*	0.9
n(He)/n(H)	0.20	0.18	0.20	0.10	0.08	0.10	0.10	0.08	0.10
log n(Si)/n(H)	-4.49	-4.49	-4.49	-4.79	-4.81	-4.79	-4.79	*-4.79*	-4.79
ξ (km s^{-1})	10	10.2	10	15	15	15	6.0	7.3	6.0
$v \sin i$ (km s^{-1})	50	48 ± 2	48 ± 2	50	48 ± 4	48 ± 4	50	51 ± 1	51 ± 1
$v_{\rm macro}$ (km s^{-1})	20	29 ± 4	29 ± 4	30	33 ± 2	33 ± 2	10	30 ± 1	30 ± 1
time (s)	142			494			2344		
checked models	10			21			128		
	Dataset D			Dataset E			Dataset F		
$T_{\rm eff}$ (K)	21,120	20,985	21,000	15,100	15,030	15,000	11,880	*11,500*	11,500
$\log g$ (cgs)	3.98	*4.0*	4.0	1.83	*1.80*	1.8	2.43	*2.3*	2.3
$\log Q$ (char)	b	*b*	b	A	*A*	A	a	*O*	O
β	1.42	*2.0*	1.2	2.8	*3.0*	3.0	1.02	*0.9*	0.9
n(He)/n(H)	0.14	0.11	0.10	0.08	0.09	0.10	0.18	0.20	0.20
log n(Si)/n(H)	-4.85	-4.80	-4.79	-4.23	-4.16	-4.19	-4.49	*-4.19*	-4.19
ξ (km s^{-1})	12	15.7	15	11	10.6	10	9	6.3	6
$v \sin i$ (km s^{-1})	50	52 ± 6	52 ± 6	50	50 ± 7	50 ± 7	50	54 ± 1	54 ± 1
$v_{\rm macro}$ (km s^{-1})	40	33 ± 5	33 ± 5	10	39 ± 7	39 ± 7	70	67 ± 7	67 ± 7
time (s)	174			392			1254		
checked models	10			26			95		
	Dataset G			Dataset H			Dataset I		
$T_{\rm eff}$ (K)	24,800	24,650	25,000	18,600	18,392	18,500	10,910	*11,000*	11,000
$\log g$ (cgs)	3.33	*3.3*	3.3	2.78	*2.8*	2.8	1.72	*1.8*	1.8
$\log Q$ (char)	B	*B*	B	O	*A*	A	C	*C*	C
β	1.1	*1.2*	1.2	1.0	*0.9*	0.9	2.10	*2.0*	2.0
n(He)/n(H)	0.11	0.12	0.10	0.14	0.13	0.15	0.11	0.09	0.10
log n(Si)/n(H)	-4.52	-4.48	-4.49	-4.25	-4.22	-4.19	-4.67	*-4.79*	-4.79
ξ (km s^{-1})	13	13.5	12	4	3.3	3	7	8.6	10
$v \sin i$ (km s^{-1})	30	30 ± 1	30 ± 1	30	30 ± 1	30 ± 1	30	30 ± 1	30 ± 1
$v_{\rm macro}$ (km s^{-1})	15	12 ± 4	12 ± 4	15	20 ± 7	20 ± 7	15	0	0
time (s)	2119			2284			356		
checked models	66			67			15		

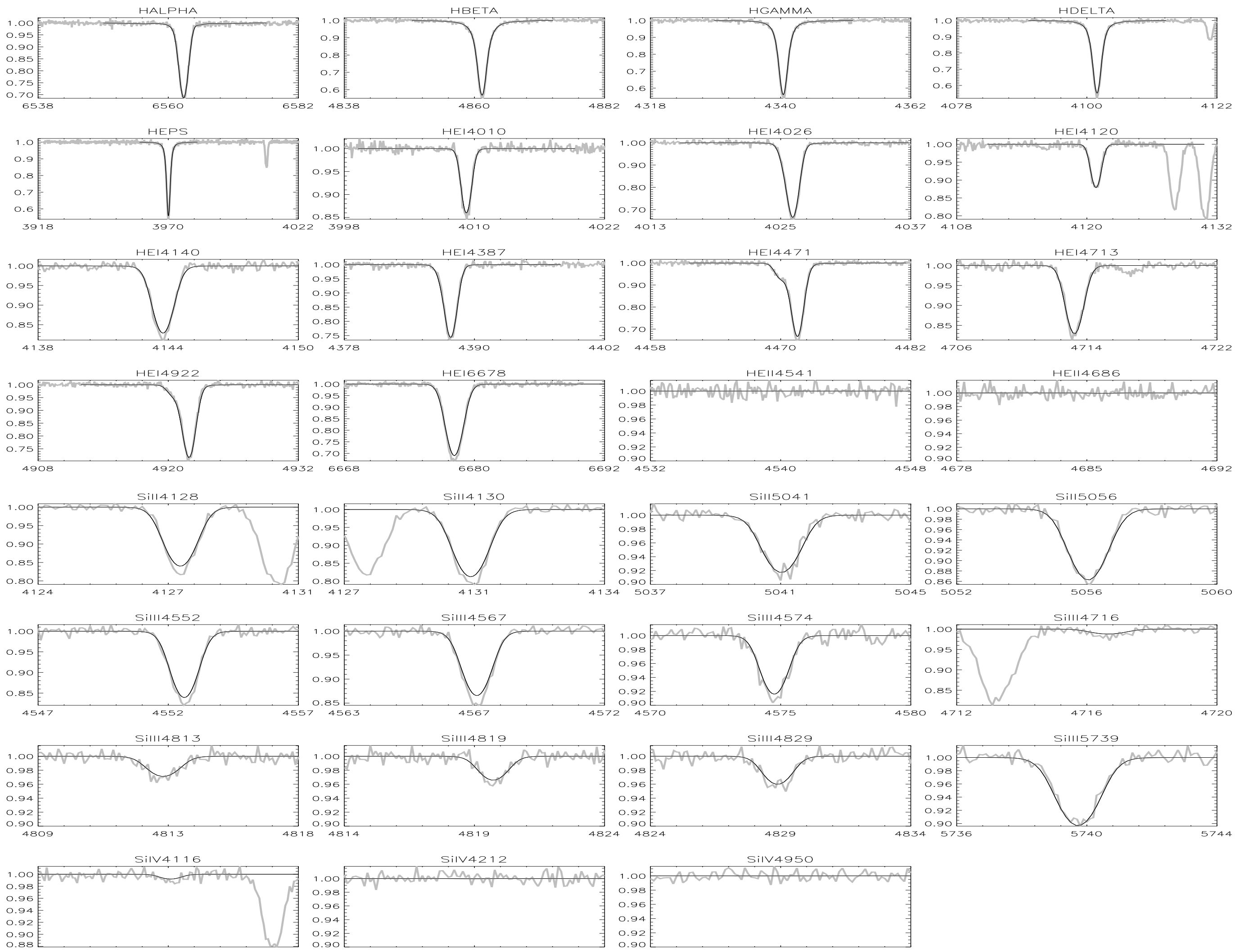

Figure A.1. Example of the fit quality for dataset E. The slight discrepancy in the cores of the Si lines arises from the difference in Si abundance between the interpolated value (log n(Si)/n(H) = -4.16) and the closest grid value (log n(Si)/n(H) = -4.19)

a justifiable approach by comparing, for multiple line profiles of stars with completely different properties, the equivalent widths computed from a Gaussian fit to the observed line profiles with those computed from a proper integration of the line pixel values. This comparison resulted in a minimal difference between both approaches. Some lines obviously cannot be fitted by a Gaussian, e.g., the He lines with a strong forbidden component in their blue wing or Stark-broadened lines such as those from hydrogen. The EW of such lines are determined by proper integration. In all other cases, where the line profile *is* well-represented by a Gaussian fit, the the observed EW is given by the integral of the Gaussian profile.

The main source of *uncertainty in the EW determination* is introduced by the noise and its influence on the exact position of the continuum within the noise. To account for this we multiplied the continuum by a factor (1 ± 1/SNR), performed a new Gaussian fit through both shifted profiles and measured the difference in EW. Note that, by considering a constant factor over the full line profiles (using the signal at continuum level), we implicitly give an equal weight to each wavelength point, even though, in reality, 1/SNR may be slightly larger in the cores, since it is proportional to $\sqrt{1/S}$, with S the obtained signal at these wavelengths. When the user deems it necessary, (s)he can apply a correction for the continuum level by a local rerectification, e.g., in the case that the normalization performed over a large wavelength range is locally a bit offset. If the offset is different on the blue and red side of the line, then the factor should be wavelength dependent. Therefore, we allow for a linear rerectification by a factor $a\lambda + b$. Another source of uncertainty in the EW is introduced by using a Gaussian fit to estimate the EW. Each of the above factors have been included in the total error budget of the EW.

Determination of $v \sin i$ (see Fig. B.3). The determination of the projected rotational velocity is the last step in the preparation of the input for AnalyseBstar. We use the semi-automatic tool developed by Simón-Díaz & Herrero (2007) to derive the projected rotational velocities (see Fig. B.3). We refer to their paper for a thorough discussion. We use the fol-

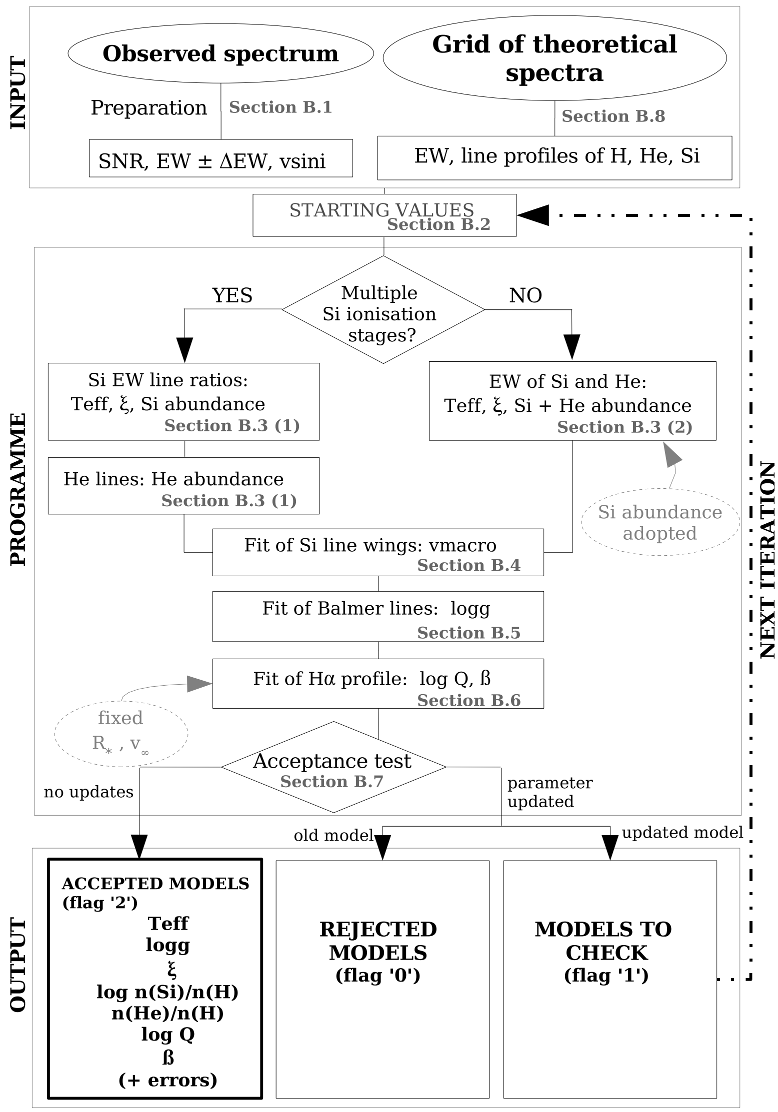

Figure B.1. Context diagram of AnalyseBstar. For a detailed explanation, see text.

lowing, least blended, metallic lines for the determination of $v \sin i$: Si II 5041, Si III 4567, 4574, 4813, 4819, 4829, 5739, C II 4267, 6578, 6582, 5133, 5145, 5151 and O II 4452. We carefully checked visually that blended lines were not taken into account. The projected rotational velocity $v \sin i$ of the star is calculated as the mean of the values derived from each individual line, and its uncertainty as the standard deviation.

B.2. Fit parameters and their starting values

Once all preparation is finished, the automatic procedure to obtain accurate values for all physical fit parameters can be started. This procedure follows an iterative scheme as outlined in Fig. B.1. In each iteration, the fundamental parameters are improved in the following order. First of all, the effects of the effective temperature, the Si abundance and the microturbulence on the Si lines are separated. Then, the He abundance is fixed using all available He lines. Next, the macroturbulent velocity is determined from well-chosen, user supplied Si lines. Then, the surface gravity is determined from the wings of Hγ, Hδ and, in the case of weak winds, also Hβ, after which the wind strength log Q ($Q = \dot{M}/(v_\infty R_*)^{1.5}$, with $\dot{M}$, the mass loss, v_∞, the terminal wind velocity, and R_*, the stellar radius) and the wind velocity exponent β are determined in parallel using Hα. Obviously, to start the iterative procedure, we need an initial guess for each of these parameters. This initial value can either be user supplied or standard. If no value is set by the user, then the following initial values are considered. The initial effective temperature will be determined from the spectral type of the star. Immediately after the rotational and macroturbulent velocities have been determined, a start value for the surface gravity is derived by running the subprocedure for the determination of the gravity (see Section B.5). For the He and the Si abundance, we have taken the lowest value as start value. We initialize the wind parameters at the lowest values, which means negligible wind, at log Q = -14.30 and β = 0.9. These are reasonable assumptions for dwarfs, which comprised the largest part of our sample. These starting values can easily be

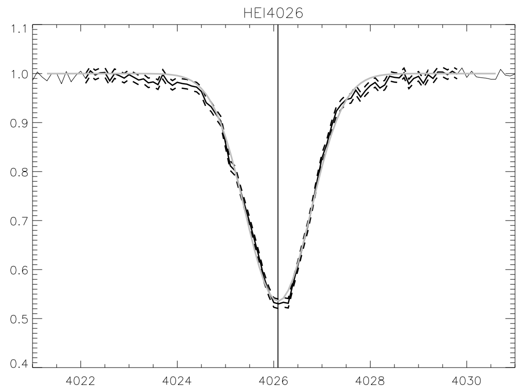

Figure B.2. Illustration of the EW determination for He I 4026. After the manual identification of the wavelength interval of the spectral line (thick black profile), a Gaussian fit to the observed line profile is made to determine the EW of the line (thick grey profile). Also indicated are: the center of the line (vertical line) and the 'shift' in flux, upwards and downwards (dashed line profiles), used to account for the noise level in the determination of the EW. Also to these line profiles a Gaussian fit is made, but these are omitted here for the sake of clarity.

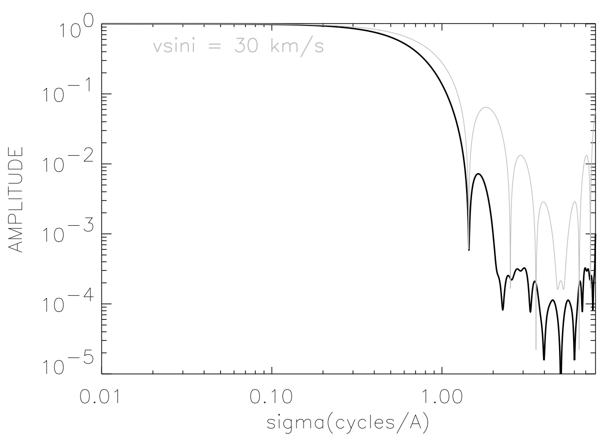

Figure B.3. Illustration of the determination of $v \sin i$ from the first minimum in the Fourier transform of the selected line profile, as implemented and described by Simón-Díaz & Herrero (2007). The user can make several attempts and finally decide which $v \sin i$ gives the best match. The difference in the slope of the first decay gives an indication of the macroturbulence. The Fourier transform of the observed line profile is indicated in black. The user indicates the first minimum in the black profile, which gives the projected rotational velocity. The Fourier transform of the rotational profile at this *vsini* is indicated in grey.

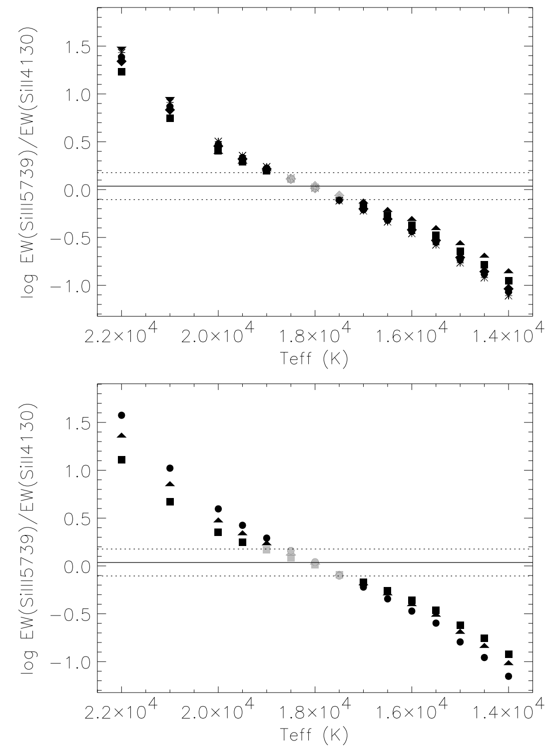

Figure B.4. Synthetic simulation of the effect of the microturbulence (top) and the Si abundance (bottom) on the logarithmic EW ratios of Si lines of different ionization stages. This example gives the (synthetic) EW ratio of Si III 5739 to Si II 4130 against a selected range of effective temperatures, for a fixed surface gravity ($\log g = 2.5$) and wind parameters ($\dot{M}$ = $0.144.10^{-7} M_{\odot}$/yr, v_{∞} = 500 km s^{-1}, $\beta = 0.9$). The ratios are evaluated for the different possibilities of the microturbulence, for a Si abundance fixed at -4.79 (upper panel: ξ = 3, 6, 10, 12, 15 and 20 km s^{-1}; triangle up, square, diamond, circle, asterisk, triangle down, respectively) and for the different possibilities of the Si abundances, for a microturbulence fixed at 10 km s^{-1} (log n(Si)/n(H) = -4.79, -4.49 and -4.19: circle, triangle up and square, respectively). The horizontal lines show the observed EW ratio and its corresponding uncertainty region. Acceptable EW ratios, which fall within these boundaries, are indicated in grey.

adapted when samples of stars with different stellar properties are aimed at. The macroturbulent velocity is initially zero, whereas for the microturbulent velocity we took a medium value of all considered possibilities, i.e., 10 km s^{-1}. The convergence speed depends on how far away the initial values are from the final solution.

B.3. Determination of the effective temperature, microturbulence and abundances

The Si lines serve multiple purposes. By using a well-defined scheme (somewhat similar to the conventional 'curve of growth' method (Gray 1976) and described, e.g., by Urbaneja 2004), we are able to separate the effects of the effective temperature, the Si abundance and the microturbulence on the line profiles, and derive an accurate value for them. Our method automatically determines from the observed spectrum which lines will be used for this purpose. The lines should be well visible (i.e. clearly distinguishable from the noise in the continuum) and the relative error on their equivalent width is typically below 10 to 15%, depending on the combination of the

temperature and the specific line considered. Whenever the relative error on its equivalent width exceeds 75%, the spectral line will be excluded in the following procedures. Such large errors are a rare exception and only occur for the weakest lines, which almost disappear into the noise level.
Basically, we can discern two different cases, namely when multiple and consecutive ionization stages of Si are available, or when there is only one ionization stage of Si. Each needs a different approach, as we will explain now.

Method 1: In case there are multiple ionization stages of Si available, we can, to first order, put aside the effect of the Si abundance by considering the EW ratios of two different Si ionization stages, as the Si abundance affects all Si lines in the same direction. For each effective temperature point in the grid, the ratios of the observed equivalent widths of Si IV to Si III and/or Si III to Si II are compared to those obtained from the model grid, given a certain $\log g$ and wind parameters (see Fig. B.4). For each combination of Si IV/III and/or Si III/II lines, this results in a range of 'acceptable' effective temperatures for which the observed EW ratio is reproduced, within the observed errors (indicated as grey symbols in Fig. B.4). From the different line ratios, slightly different temperatures may arise. Under the assumption that $\log g$ and the wind parameters are perfectly known, the combination of all these possibilities constitutes the set of acceptable effective temperatures.

Once we have a list of *acceptable* temperatures, we can derive for each temperature the best microturbulent velocity and the best Si abundance, by analyzing the variation in equivalent width of different lines as a function of these quantities. In what follows, we describe the full process, step by step:

- *Step 1: Deriving the abundances for each microturbulence, line by line*
  In this first step, the observed EW of each Si line is compared to the set of theoretically predicted EWs corresponding to the available combinations of Si abundance and microturbulence in the grid (see Fig. B.5). For each microturbulent velocity (and for each Si line), we look for the range of Si abundances that reproduce the observed EW, within the observed errors. This is done through linear interpolation. Note that this gives us only an approximative estimate of the Si abundance. Indeed, as can be seen in Fig. B.5, the change in EW with increasing microturbulence is marginal for weak lines, but increases for stronger spectral lines, indicating that we may no longer be in the linear part of the curve of growth.
- *Step 2: Deriving the mean abundance for each microturbulence and the slope of the best fit*
  In a second step we compare, for each microturbulence, the abundances (with the derived uncertainties) found in step 1 to the observed EW of each line (see Fig. B.6). Since a star can only have one Si abundance, we should find the same Si abundance from all the different Si lines, i.e. the slope of the best fit to all the lines should be zero. From the different abundances derived from each line, we can calculate the mean abundance for each microturbulence.
- *Step 3: Deriving the 'interpolated' microturbulent velocity*
  In a third step, we investigate the change of the slope when varying the microturbulence (see upper panel Fig. B.7). Through linear interpolation, we find the microturbulence for which the slope would be zero (i.e. for which the Si abundance derived from each line separately would be the same). This is the estimated 'interpolated' microturbulence.
- *Step 4: Deriving the 'interpolated' abundance*
  Using now the relation between the microturbulence and the mean abundance derived in step 2, we interpolate to find the estimated 'interpolated' Si abundance at the estimated 'interpolated' microturbulence found in step 3 (see lower panel Fig. B.7).
- *Step 5: Deriving the 'interpolated' effective temperature*
  Now that we obtained the estimated 'interpolated' values for the microturbulence and Si abundance, we can go back to Fig. B.4 and interpolate in two dimensions to derive a value for the effective temperature, which reproduces the observed EW. The mean of the effective temperatures from each line ratio will then be accepted as a value for the 'interpolated' effective temperature of the star.
- *Step 6: Determination of the 'closest' grid values*
  For the next steps in the automatic procedure, we will need the closest grid values to these estimated 'interpolated' values rather than the real values themselves. These closest values will constitute a new entry in the list of possibilities. If the real value for the Si abundance or microturbulence falls exactly between two grid points, both are added to the list.

We repeat these steps for each 'possible' grid temperature, initially derived from Fig. B.4 (grey symbols), and obtain in this way a set of new possible solutions that optimally reproduce the Si lines. Temporarily fixing the values for $T_{\rm eff}$, ξ, log n(Si)/n(H) in the way described above leads to a new estimate for the He abundance, denoted as n(He)/n(H). As for the Si abundance, we only consider three different values. We apply a similar method as for the determination of the Si abundance, in the sense that we derive the best-suited abundance from each line separately, and take the mean value as the 'interpolated' value. Figs B.8 and B.9 illustrate this process. Note that we intrinsically assume that the microturbulence is the same throughout the atmosphere, i.e. that there is no radial stratification. In this way, the microturbulence, necessary to account for the broadening in the He lines, will be assumed to be the same as the one derived from the Si lines. Note also that the uncertainty in the derived He abundance will be larger when the He abundance is lower than 0.10. Indeed, in this case we are forced to extrapolate to a region where it is unclear how the dependence of the equivalent width with abundance will change. The decrease towards abundances lower than solar may be steeper or follow a logarithmic trend, in which case the predicted values would be underestimated. In this case we can only state that the solar abundance is an upper limit of the true abundance. Values lower than the primordial He abundance of $\sim$0.10 can no longer be considered physical, except when diffusion effects start to play a role and He settles. In that case, the He abundance observed at the stellar surface could be lower. Such chemically peculiar stars are referred to as He weak stars and are usually high-gravity objects. Helium settling was not taken into account in our models.

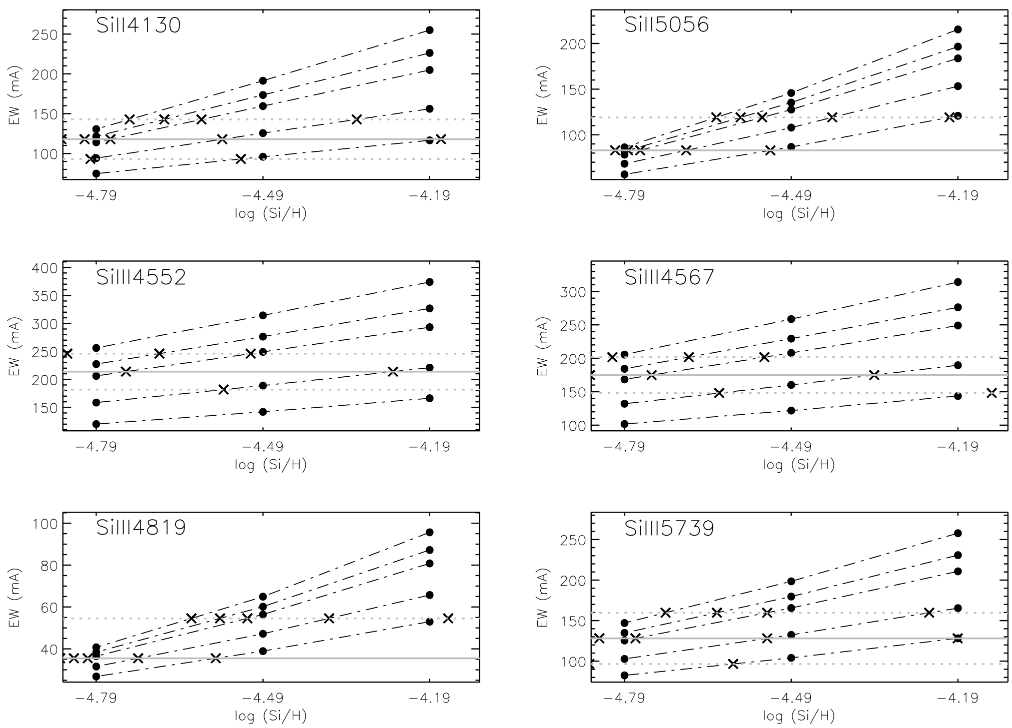

Figure B.5. Step 1 (for each $T_{\rm eff}$ and for each line): For each of the five considered microturbulent velocities (5 dash-dotted lines, from low EW to high EW: 3, 6, 10, 12, 15 km s^{-1}), we derive the Si abundance that reproduces the observed EW (horizontal grey lines) of the spectral line through linear interpolation. The Si abundances and the corresponding upper and lower limit are represented by the crosses. The displayed example is a synthetic simulation. Only a selection of lines is shown. Usually many more lines can be used. In this example, no Si IV was "observed", so only Si II and Si III were considered.

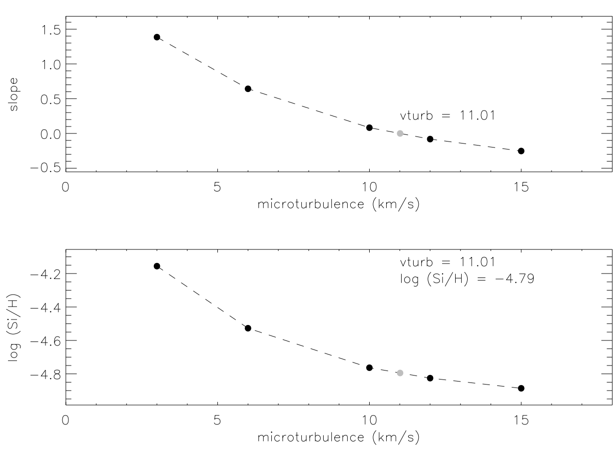

Figure B.7. Steps 3 & 4: the 'interpolated' microturbulent velocity and the accompanying 'interpolated' Si abundance (indicated in grey) are derived from the position where the slope of the best fit (step 2) is zero. The Si abundances, given in the lower panel, are the *mean* abundances derived in step 2. The displayed example is a synthetic simulation.

Method 2: In case there is only one ionization stage of Si available (mostly for late B-type stars, for which we only have Si II, but also for few hotter objects around $T_{\rm eff}$ = 23 000 K ± 3000 K with Si III) only, we can no longer use the ionization balance to derive information about the effective temperature, independent of the abundances of He and Si, and independent of the microturbulence. Indeed, we have only two *known* factors (in the case of late B-type stars: EW of He I and EW of Si II) to derive four *unknown* parameters ($T_{\rm eff}$, ξ, log n(Si)/n(H), n(He)/n(H)). Fortunately, we can constrain the effective temperature quite well. For instance, in the cold B-type domain, He I is very sensitive to changes in effective temperature (see, e.g., Fig. 2 in Lefever et al. 2007a), which means that we can use the joint predictive power of He I and Si II to derive a set of *plausible* values for $T_{\rm eff}$. This is done by comparing the theoretical EWs of all combinations of Si abundance, microturbulence and effective temperature (within a range ± 4 000 K around the currently investigated $T_{\rm eff}$) with the observed EWs, and selecting the 'best' combinations from an appropriate log-likelihood function (for details, see Lefever 2007). This method does not only work for the cool domain, but also for those hotter objects where only Si III is present, in this case because the EW of Si III varies much faster than the EW of He I.

For each of the derived *plausible* $T_{\rm eff}$ values, we still have to find the corresponding Si (from the Si lines) and He abundances (from the He lines), and the microturbulence (from the Si and/or He lines). As the He lines are liable to Stark broadening, we use only Si lines to derive the microturbulent broadening. This means that we essentially have to derive only three unknown parameters from two known data: two from the

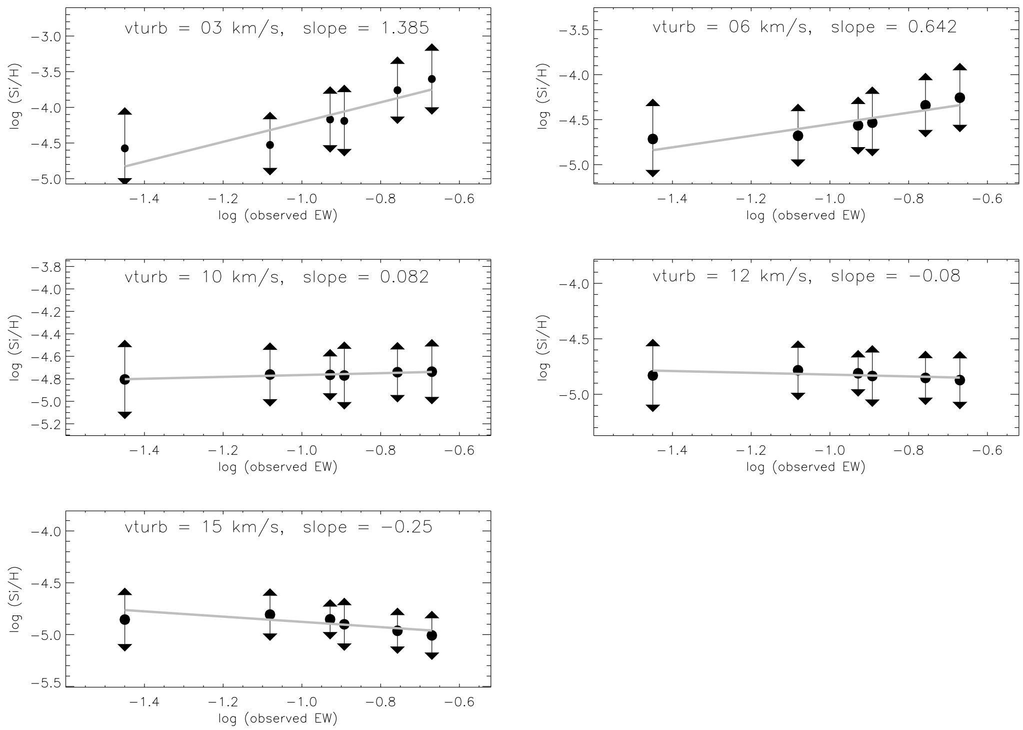

Figure B.6. Step 2 (for each microturbulence): we plot the Si abundances and their uncertainties for all 6 lines for which we derived these values in step 1, as a function of the observed EW. The least squares fit to the abundances are shown in grey. The microturbulent velocity for which the slope of this fit is zero (i.e. equal abundance from each line) gives an estimate of the 'interpolated' microturbulent velocity. The displayed example is a synthetic simulation.

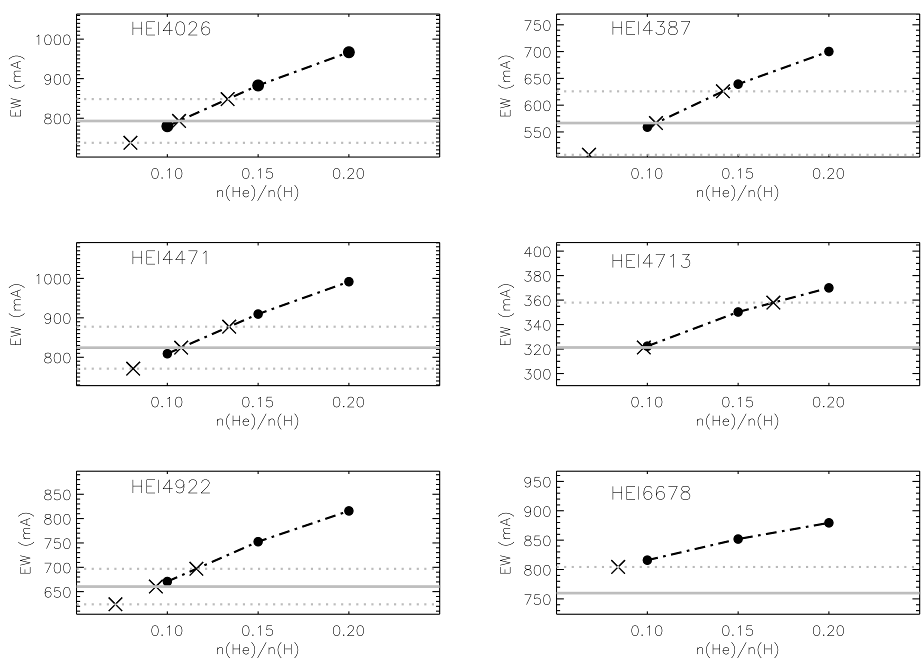

Figure B.8. For each He line, the most suited He abundance is derived through interpolation. The theoretically predicted values are shown as filled circles, the interpolated values as crosses. The horizontal lines indicate the observed equivalent width and the observed errors. The displayed example is a synthetic simulation.

Si lines (log n(Si)/n(H) and ξ), and one more from the He lines (n(He)/n(H), assuming that the microturbulence in Si and He is similar), which still leaves us with one free parameter for which we will have to make an assumption in order to be able to fix the other two. We have chosen to 'fix' the Si abundance, as it has no direct influence on the He lines. However, we *do* consider each of the three possibilities for the Si abundance in the grid, i.e., we consecutively consider the three cases in which Si is depleted, solar and enhanced. This allows us to determine also the microturbulent velocity, which is consequently used to fix the He abundance from the He lines.

To finally decide which of the various combinations matches the observations best, a twofold check is applied. (i) all profile-sets are inspected by eye (this, again, compromises a fully automatic procedure), since parameter combinations leading to obvious mis-fits can be clearly excluded on this basis. (ii) Again, a log-likelihood procedure is used to find the best matching model among the list of final solutions, combining the likelihoods of the EWs of the Si/He lines and of the profile shapes of *all* lines, respectively (see Lefever 2007).

Even though, with this procedure, we are able to derive reasonably good estimates for most of the stellar/wind parameters, we have no means to restrict the Si abundance in a reliable way as it is possible within 'method 1'. The outcome of maximizing the log-likelihood can give us only a general idea of the abundance, but still leaves us with a larger uncertainty, which has been accounted for in the adopted error budget (see Table 3).

B.4. Macroturbulence $v_{\rm macro}$

The macroturbulence considered is characterized by a radial-tangential model (Gray 1975). In this model a time-independent velocity field is assumed to be active and modeled by assuming that a fraction (A_r) of the material is moving radially while the complementary fraction moves tangentially (A_t). In our model for $v_{\rm macro}$, we use the standard assumption that the radial and the tangential components are equal in fraction. Assuming additionally that the distribution of the velocities in the radial and the tangential directions are Gaussian, the effect of macroturbulence can be introduced in the synthetic line profiles by means of a convolution with a function, which consists of a Gaussian and an additional term proportional to the error function (see equation (4) in Gray 1975). It changes the shape of the line profile, but leaves the equivalent width untouched.

Only weak lines should be used to determine $v_{\rm macro}$. For B-type stars, Si lines are the best suited, since they most obviously show the presence of $v_{\rm macro}$ in their wings. The user decides which Si lines should be used throughout the full process. To determine the strength of $v_{\rm macro}$, we convolve the Si profiles of the (at that instant) best fitting model with different values of $v_{\rm macro}$[7]. The consecutive values considered for the convolution are chosen using a bisection method, with initial steps of 10 km s^{-1}. The bisection continues as long as the stepsize is larger than or equal to 0.1 km s^{-1}, which will be the final precision of the $v_{\rm macro}$ determination. For each considered $v_{\rm macro}$-value, we compute its log-likelihood in order to quantify the difference between the obtained synthetic profile and the observed line profile, as follows:

$$l \equiv \sum_{i=1}^{n}\left[-\ln(\sigma) - \ln(\sqrt{2\pi}) - \frac{1}{2}\left(\frac{y_i-\mu_i}{\sigma}\right)^2\right], \qquad \text{(B.1)}$$

with n the considered number of wavelength points within the line profile, y_i the flux at wavelength point i of the observed line profile, μ_i the flux at point i of the synthetic profile (convolved with the $v_{\rm macro}$ under consideration), and σ the noise, i.e. 1/SNR, of the considered line profile. A thorough discussion of why this particular likelihood function is suitable for spectral line fitting can be found, e.g., in Decin et al. (2007).

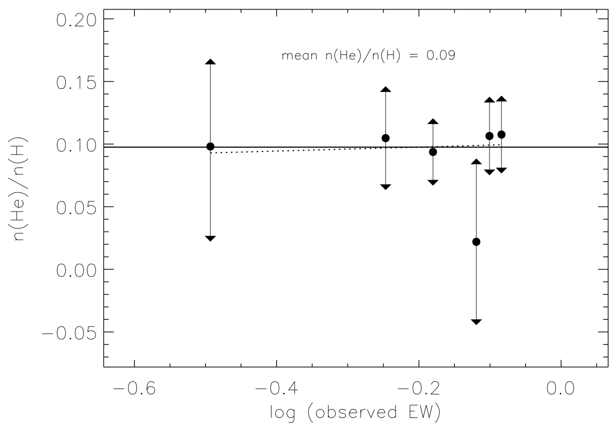

Figure B.9. The finally provided He abundance is calculated as the mean over all lines. The abundance derived from each line separately is represented by the filled circles, while the arrows show the derived errors. The best linear fit is indicated as the dotted line, while the horizontal solid line shows the mean value. The displayed example is a synthetic simulation.

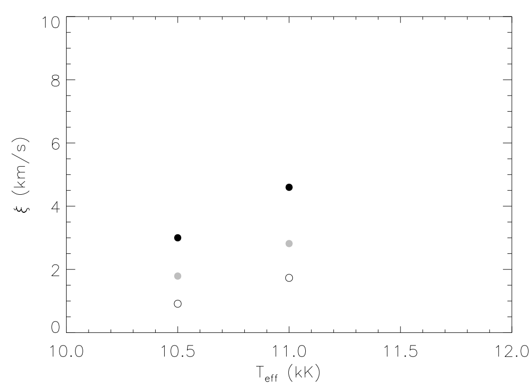

Figure B.10. Once a set of possible effective temperatures is fixed from the joint predictive power of He I and Si II (see text), we can determine for each of these temperatures (in this case: 10 500 and 11 000 K) the correct microturbulence, under the assumption that we know the Si abundance. Resulting combinations are shown for log n(Si)/n(H) = −4.19 (open circles), −4.49 (grey filled circles) and −4.79 (black filled circles). The displayed example is a synthetic simulation.

[7] At this point the profile has already been convolved with the appropriate rotational and instrumental profiles.

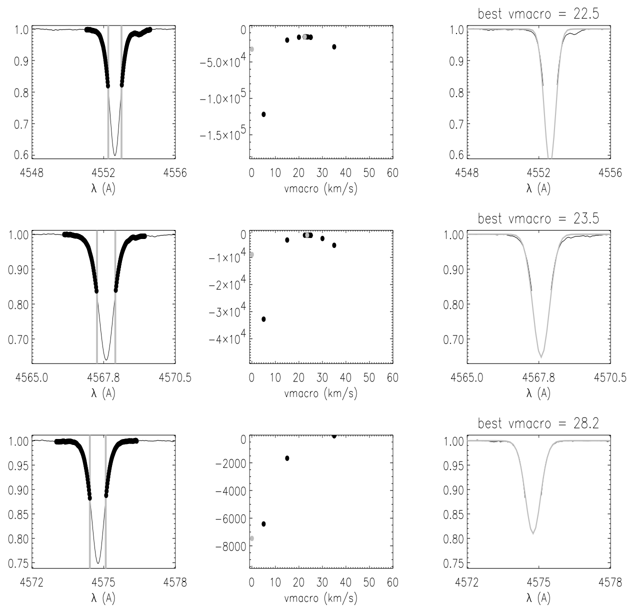

Figure B.11. Determination of the macroturbulent velocity of β CMa for three different Si lines. The panels should be read from left to right as follows.
Left: The left and right edge of the line region (i.e. outermost dots at continuum level) are indicated by the user at the start of the procedure. The blue and red edges (grey vertical lines) are determined as the point where the flux is half of the minimal intensity. They determine how far the wings extend towards the line center. The black dots represent the points that are finally used to determine the macroturbulence.
Middle: Obtained log-likelihood as a function of $v_{\rm macro}$ (see Eq. (B.1)). Note the broad maximum in the log-likelihood distribution, which gives rather large error bars.
Right: The fit with the best $v_{\rm macro}$ is shown as the grey profile. Note that the significant amount of macroturbulence might be explained by the fact that this star exhibits non-radial oscillations (Mazumdar et al. 2006).

The same procedure is repeated for all considered line profiles, and the mean, derived from the different lines, gives the final $v_{\rm macro}$. The error is set by the maximal deviation of the derived $v_{\rm macro}$-values from the final value. From Fig. B.11, it is clear that the shape of the log-likelihood distribution near the maximum can be quite broad, which indicates that the errors in $v_{\rm macro}$ with respect to the log-likelihood are significant.

A warning has to be made here. It was recently shown by Aerts et al. (2009) that time-dependent line profile variations due to non-radial gravity-mode oscillations, which are expected in B stars, offer a natural physical explanation for the occurrence of macroturbulence. Such oscillations disturb an appropriate estimate of $v \sin i$, both from the Fourier method and from a goodness-of-fit approach. The only way to assess the effect of oscillations on the $v \sin i$ determination is by taking an appropriate time series of line profile variations (e.g., Aerts & De Cat 2003). Luckily, an inappropriate $v \sin i$ estimate, accompanying a line profile fit in terms of $v_{\rm macro}$, does not have a serious effect on the determination of the other parameters of the star from snapshot spectra, such that the approach implemented in AnalyseBstar is valid as long as the values of $v \sin i$ and $v_{\rm macro}$ are not used for physical interpretations. A large value for the macroturbulence is an indication that time-dependent pulsational broadening may occur in the star under investigation.

B.5. Surface gravity $\log g$

The surface gravity $\log g$ is the result of fitting the Balmer lines. We mainly use Hγ and Hδ, possibly complemented with Hβ in case of weak winds (i.e. if log Q ≤ -13.80). Since Hϵ is somewhat blended, and the merging is not always reliable for this region (see above), this line will not be used as a primary gravity determinator, but will only serve as an additional check (together with Hβ, in case of stronger winds). Since we want to define the profile only from the extreme wings down to the strongest curvature (see discussion of the different contributions below), we excluded the central part of the line, accounting for several mechanisms, which affect the core of the Balmer lines to some extent, e.g., rotation, micro- and macroturbulence and thermal broadening. Once we removed the inner part of the line profile, we compare the observed Balmer lines with the synthetic line profiles, by considering all possibilities for $\log g$ which are available at this given effective temperature gridpoint. We decide which gravity is the best, by maximizing its log-likelihood (see Eq. B.1), calculated over all Balmer lines. With this procedure, we encountered the following problem: Hγ and Hδ (our main gravity indicators) can sometimes be seriously affected by a large amount of blends. Ignoring them can lead to a serious overestimation of the gravity, since the log-likelihood function will take all these blends into account (see Fig. B.12). Therefore, we developed a procedure to find the “line continuum”, cutting away the blends. The procedure is basically a sigma-clipping algorithm which keeps only those points that have a flux higher than both neighboring points (the so-called ‘high points’) and where, at the same time, the difference is less than 1/SNR. After removing all other flux points, only the “line continuum” is left (see middle panel Fig. B.12). We interpolate this continuum to obtain the flux at all original wavelength points, and the inner part of the line is added again (i.e. the part between the last blend in the blue wing and the first blend in the red wing, but obviously still without the central core). Also all original flux points which deviate by less than 1/SNR from the interpolated “line continuum” are included again. In this way we keep only the flux points which really determine the shape of the wing to fit the synthetic Balmer wings, and we are able to determine an accurate value for $\log g$ (see right panel Fig. B.12). We realize that some points that may be marked as local continuum in this way, may still be lower than what the real local continuum level would be, because of the transition of one blend into another. However, this will only be the case for very few points, which will give no significant weight to the log-likelihood.

The finally accepted surface gravity will be this $\log g$ which gives the best fit to *all* selected Balmer lines simultaneously. Half the gridstep in $\log g$ could thus be considered a good er-

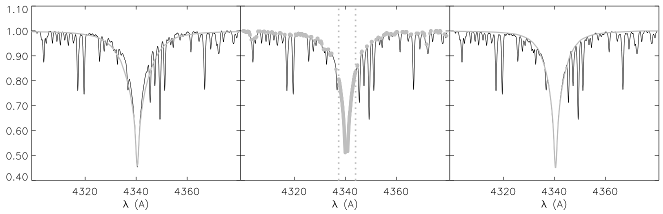

Figure B.12. Illustration of the effect of blends on the determination of log g, and the clipping algorithm to improve the fit, for β CMa. Left: The many blends in the wings of the profile prevent an accurate least squares fit and lead to too broad wings, implying too high a gravity. Central: From the observed line profile (black), only the 'high points' (grey dots), which deviate less than 1/SNR from their neighbors, are kept, complemented with the inner part of the line between the last blend in the blue wing and the first blend in the red wing (indicated as grey vertical lines), but still excluding the central core, which is affected by several broadening mechanisms. Right: After the removal of all blends through sigma clipping (see text), we are able to obtain a good representation of the line wings (grey profile) and, therefore, to derive a very accurate value for the gravity.

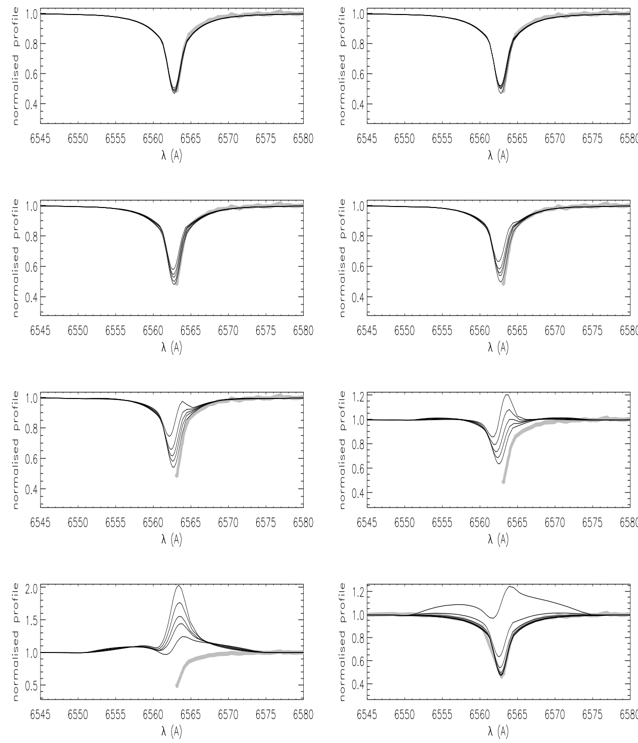

Figure B.13. (Synthetic simulation) For each different wind strength parameter log Q (7 values, from left to right and from top to bottom: log Q $=$ $-14.30, -14.00, -13.80, -13.60, -13.40, -13.15, -12.70$), we search for the best β (in each panel, the 5 different values for β are indicated: 0.9, 1.2, 1.5, 2.0, 3.0) by comparing only the red wing (grey part of the profile). Then the synthetic profiles of each best (log Q, β) combination are compared to the entire Hα profile (bottom right).

ror estimate. However, to account for the coupling with $T_{\rm eff}$, we consider 0.1 dex as a more appropriate error. This gravity should be corrected for centrifugal acceleration ($\rightarrow \log g_c$) due to stellar rotation by a factor $(v \sin i\,)^2/R_*$, when calculating, e.g., the mass of a star (Repolust et al. 2005, and references therein).

B.6. Wind parameters

A change in mass loss rate will mainly affect the shape of Hα. For cool objects and weak winds, Hα is nearly 'photospheric' and will, in essence, be an absorption profile, with more or less symmetric components, since the 're-filling' by the wind is low. In case of stronger winds, Hα will take the shape of a typical P Cygni profile. For hot objects, where Hα is dominated by recombination processes, and high mass-loss rates, the profile may even appear in full emission.

The wind parameter β determines the velocity law, which directly influences the density. The red wing of Hα is well suited to determine β, since it is formed by emission processes alone, averaged over the receding part of the (almost) complete wind. For a fixed mass loss, a 'slower' velocity law (i.e., a higher β value) will result in higher densities in the lower atmosphere, close to the star. This enlarges the number of emitted photons with velocities close to the line center, resulting in more emission. Around the central wavelength, the absorption component of the line profile refills and the emission component becomes stronger. Therefore the slope of the red wing of the P Cygni profile becomes steeper. In this sense, the steepness of the red wing is a measure for the value of β.

We estimate the wind parameters log Q and β by comparing the observed Hα profile with the different synthetic Hα profiles by making combinations of log Q and β. We decided to make the determination of the wind parameters not too sophisticated, by simply using the best values for log Q and β available in the grid, without interpolation and further refinement. Once we have selected for each log Q the best β, we decide on the best combination by considering the best fit to the entire profile.

B.7. Some final remarks

At the end of this iteration cycle, an acceptance test is performed. When the method can run through the whole cycle without needing to update any of the fit parameters, the model is accepted as a good model, and gets the flag '2'. If a better model was found (i.e., when one or more parameters changed), the initial model is rejected and gets flag '0', whereas the improved model is added to the list of possibilities, and gets flag '1' (cf. 'models to check' in the flowchart diagram, Fig. B.1). As long as the list with possibilities with flag '1' is not empty, the parameters of the next possibility are taken as new starting values.

Line profile fits are always performed allowing for a small shift in wavelength, or radial velocity (5 wavelength points in either direction, corresponding to typically 5 km s^{-1}), to prevent flux differences to add up in case of a small radial velocity displacement.

B.8. The underlying FASTWIND BSTAR06 grid

Even though the majority of the CoRoT targets consisted of late B-type stars, we nevertheless invested in a grid which covers the complete parameter space of B-type stars. In this way, we hoped to establish a good starting point for future (follow-up) detailed spectroscopic analysis of massive stars. The grid has been constructed as representative and dense as possible for a wide variety of stellar properties within a reasonable computation time. Hereafter we give a short summary of the considered parameters. For a more detailed description, we refer to Lefever et al. (2007a).

- 33 *effective temperature* ($T_{\rm eff}$): from 10 000 K to 32 000 K, in steps of 500 K below 20 000 K and in steps of 1 000 K above it.
- on average 28 *surface gravities* ($\log g$) at each effective temperature point: from $\log g$ = 4.5 down to 80% of the Eddington limit
- 1 'typical' value for the *radius* (R_*) for each ($T_{\rm eff}$, $\log g$)-gridpoint: approximative value from interpolation between evolutionary tracks, keeping in mind that a rescaling to the 'real' value is required when analyzing specific objects. Indeed, the real radius can then, in most cases, be determined from the visual magnitude, the distance of the star and its reddening, and from the theoretical fluxes of the best fitting model.
- 3 values to fix the *chemical composition*: n(He)/n(H) = 0.10, 0.15, and 0.20, and log n(Si)/n(H) = -4.19, -4.49, and -4.79 (i.e. enhanced, solar, and depleted). The background elements (responsible, e.g., for radiation pressure and line-blanketing) were assumed to have a solar composition.
- 7 values for the *wind-strength* parameter log Q
- 1 'typical' value for the *terminal wind velocity* (v_∞): estimated from the relation between observed terminal velocity and photospheric escape velocity (Kudritzki & Puls 2000, and references therein), where the latter quantity has been calculated from the actual grid parameters ($\log g, R_*$ and $T_{\rm eff}$).